Coordination Chemistry Reviews 254 (2010) 2663–2676

Contents lists available at ScienceDirect

Coordination Chemistry Reviews

journal homepage: www.elsevier.com/locate/ccr

Review

Electronic structure and photophysics of pseudo-octahedral vanadium(III) oxo complexes☆

Kevin R. Kittilstved*, Andreas Hauser

Université de Genève, Département de chimie physique, Sciences II, 30 Quai Ernest-Ansermet, CH 1211 Genève, Switzerland

Contents

ARTICLE INFO

Article history:
Received 29 December 2009
Accepted 16 February 2010
Available online 23 February 2010

Keywords:
Vanadium(III)
Zero-field splittings
Ligand field spectroscopy
Jahn–Teller (JT) distortion
Ligand field theory

ABSTRACT

The electronic structure and the photophysical properties of the vanadium(III) ion in pseudo-octahedral oxygen coordination is reviewed. V^{3+} has received much interest from spectroscopists in recent years due to the advancement of state-of-the-art experimental techniques such as inelastic neutron scattering and high-field electron paramagnetic resonance spectroscopy that directly interrogate its large ground state zero-field splittings (ZFSs) and to rational parameterization of the ligand field parameters using the angular overlap model. However, for V^{3+} these ZFSs can be large enough to also be probed directly by high-resolution electronic absorption spectroscopy of intra-configurational ($t_{2g}^2 \rightarrow t_{2g}^2$) spin-forbidden transitions in the near-IR and visible regions. The luminescent properties of V^{3+} with hexa-oxo and tris-bidentate di-oxo-coordination are quite disappointing compared to its neighbor in the periodic table, Cr^{3+}, in similar environments. The efficient non-radiative pathways in these compounds are reviewed and compared to recent work on V^{3+} doped into $NaMgAl(ox)_3{\cdot}9H_2O$. The poor luminescence quantum efficiencies of V^{3+} oxo complexes is explained by strong coupling of multi-phonon processes with a dynamic Jahn–Teller distortion originating from the ^3E trigonal component of the $^3T_{1g}$ ground state.

1. Introduction

Trivalent vanadium has a $[Xe]3d^2$ open shell electron configuration and the ensuing many-electron states present interesting features to the coordination chemist. Accordingly, experimental studies of the electronic structure of this ion in different hexa-oxo-coordination environments are plentiful and go back to classic studies of V^{3+} in Al_2O_3 by McClure [1], $[V(urea)_6]^{3+}$ by Dingle et al. [2], $[V(OH_2)_6]^{3+}$ in the alums by Tregenna-Piggott and co-workers [3–5], and $[V(ox)_3]^{3-}$ in $NaMgAl(ox)_3{\cdot}9H_2O$ by Piper and Carlin [6,7], just to mention a few. The electronic structure of V^{3+} in Al_2O_3 and hexa-aqua coordination has also been the subject of ligand field theoretical investigations [8–12], in particular with respect to understanding spin–orbit coupling and the $^3T_{1g}$ ground state splittings [3,10,11]. Several of these systems have been reinvestigated in

☆ Dedicated to the memory of our beloved colleague and friend, PD Dr. Philip L. W. Tregenna-Piggott.

* Corresponding author at: University of Washington, Department of Chemistry, Box 351700, Seattle, WA 98195-1700, United States. Tel.: +1 509 616 8754.
E-mail address: kkittils@u.washington.edu (K.R. Kittilstved).

0010-8545/$ – see front matter © 2010 Elsevier B.V. All rights reserved.
doi:10.1016/j.ccr.2010.02.021

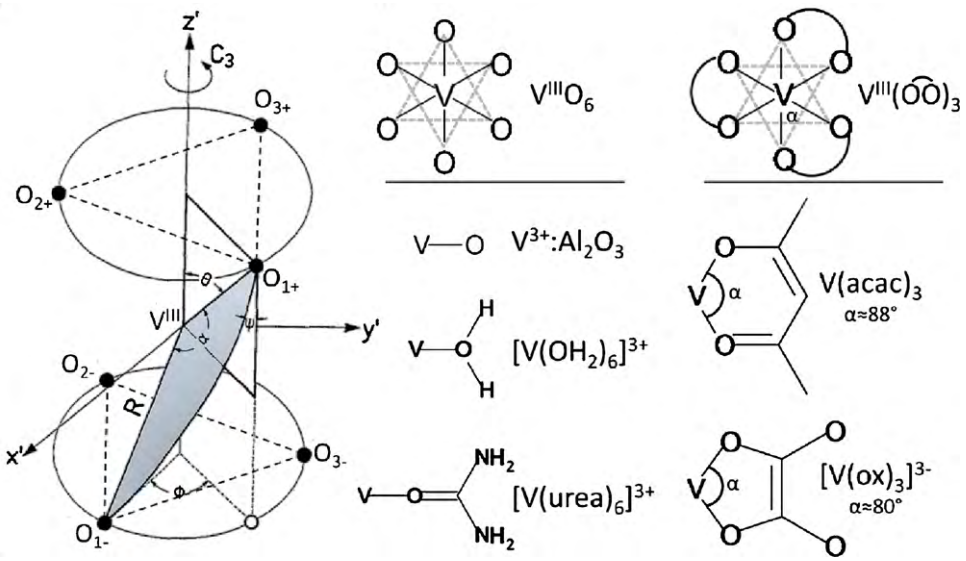

Fig. 1. (Left) Definition of the Euler angles for a model pseudo-octahedral $V^{III}O_6$ complex (adapted from [34]). Bonding of mono-dentate (center) and bidentate (right) oxo-ligators to V^{3+}. The O_{i+}–V–O_{i-} (i = 1, 2, 3) angle for $V^{III}O_6$ coordination is on average 90°. The bite angle, α, for $V^{III}(\breve{O}\breve{O})_3$ complexes is different for V(acac)$_3$ and $[V(ox)_3]^{3-}$ as a result of the difference in the number of atoms in the chelate ring; V(acac) makes a 6-membered ring, and V(ox) binding creates a smaller 5-membered ring. The strain in the 5-membered V(ox) ring cannot support the $\alpha \approx 88^\circ$ bite angle of V(acac)$_3$. Crystallography confirms the acute bite angle for $K_3V(ox)_3 \cdot 3H_2O$ of $\alpha \approx 80^\circ$ [38].

recent years in the wake of the development of new experimental techniques that directly probe the ground state zero-field splittings (ZFSs) such as high-field electron paramagnetic resonance (HFEPR), inelastic neutron scattering (INS), and low-temperature magnetic susceptibility measurements [5,13]. Alternative probes such as high-resolution electronic absorption and Zeeman spectroscopy of intra-configurational ($t_{2g}^2 \rightarrow t_{2g}^2$) spin-forbidden transitions can also provide the means to study the electronic structure of V^{3+} compounds and, under certain conditions discussed in Section 3, obtain the ground state ZFSs and g-values of both the ground and excited states [2,14–17].

In this review, we focus on the electronic structure and the photophysical properties of trigonally distorted pseudo-octahedral vanadium(III) hexa-oxo ($V^{III}O_6$) and tris-bidentate di-oxo ($V^{III}(\breve{O}\breve{O})_3$) complexes studied by spectroscopic methods. The majority of the complexes and coordination motifs discussed are shown in Fig. 1, which includes both mono-dentate ligands such as urea (O=C(NH$_2$)$_2$), water, and oxide lattices, and bidentate ligands such as acetylacetonate (acac) and oxalate (ox).

2. Theory of V^{3+} in O_6 ligand fields

In this section, we review the theoretical description and parameterization of the many-electron states arising from the d^2 electronic configuration in pseudo-octahedral ligand fields. The Hamiltonian describing the ligand field of pseudo-octahedral V^{3+} is given by

$$\mathcal{H} = \mathcal{H}_{ion} + \mathcal{H}_{O_h} + \mathcal{H}_{D_3} + \mathcal{H}_{ee} + \mathcal{H}_{so} + \mathcal{H}_{JT}, \quad (1)$$

where $\mathcal{H}_{ion}$ is the free ion Hamiltonian for the valence electrons in the central field approximation, $\mathcal{H}_{O_h}$ and $\mathcal{H}_{D_3}$ are the octahedral and trigonal ligand field operators, $\mathcal{H}_{ee}$ accounts for the electron–electron repulsion, $\mathcal{H}_{so}$ is the spin–orbit coupling operator, and $\mathcal{H}_{JT}$ describes a possible Jahn–Teller (JT) distortion. For the electronic states considered here, the JT effect is small compared to the trigonal and spin–orbit effects and for simplicity will be neglected for discussions concerning the $^3T_{1g}$ ground state in O_h symmetry. Treatment of the JT effect and its implications on the ZFS parameters has been developed fully by Tregenna-Piggott and Carver [3] and will be discussed further in Sections 3.3 and 4.1.

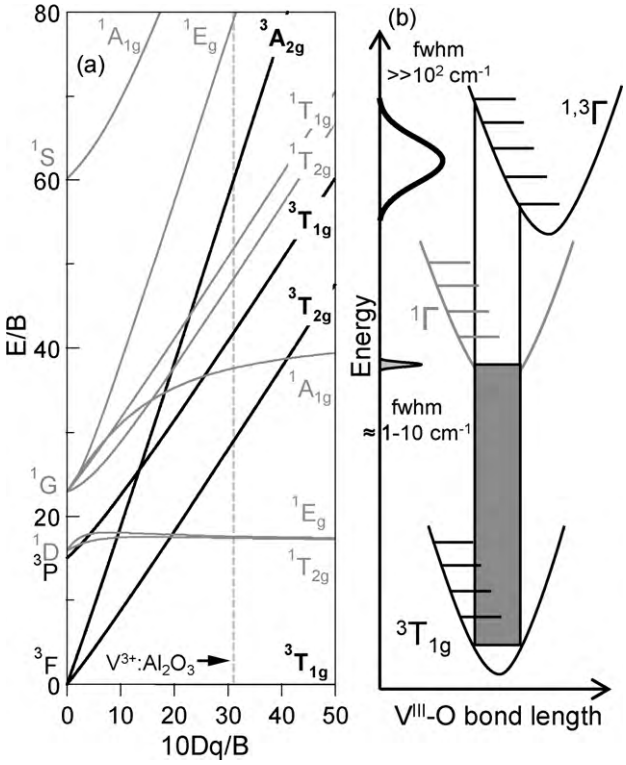

Fig. 2. (a) Tanabe–Sugano diagram for a d^2 ion in an octahedral ligand field calculated with $C = 5.4B$. Transitions are classified into three groups: spin-allowed ($^3\Gamma$, slope > 0), inter-configuration spin-forbidden ($^1\Gamma$, slope > 0), and intra-configurational spin-forbidden ($^1\Gamma$, slope ~0, including the $^1A_{1g}(^1G)$ state). The vertical dashed line at $10Dq/B \approx 31$ corresponds the ratio for V^{3+} in Al_2O_3. (b) Schematic representation of the expected band widths for intra- and inter-configurational d–d transitions. Intra-configurational spin-forbidden transitions, such as $^3T_{1g}(t_{2g}^2) \rightarrow {}^1\Gamma_e(t_{2g}^2)$, have no excited state distortion in the strong-field limit and thus have narrow line widths of the order of 1–10 cm^{-1} at low temperature. Inter-configurational spin-allowed and spin-forbidden transitions, such as $^3T_{1g}(t_{2g}^2) \rightarrow {}^{1,3}\Gamma(t_{2g}^1 e_g^1$ or $e_g^2)$, involve promotion of one or two electrons from a non-bonding t_{2g} orbital into the anti-bonding e_g orbital resulting in an elongation of the V^{III}–O bond. The difference in bond length causes a broadening of the transition line width. Typical band widths for these types of transitions are >10^3 cm^{-1}.

Table 1
Electric dipole selection rules for complexes with trigonal site symmetries of D_3, C_{3v}, and C_3. Take note that the ordering of the irreducible representations on the left side of the table is different for D_3 and C_{3v} symmetries.

D_3			A1	A2	E
	C_{3v}		A1	A2	E
		C_3	A		E
A2	A1	A	π	≠	σ
A1	A2		≠	π	σ
E	E	E	σ	σ	σ + π

The Tanabe–Sugano diagram of the V^{3+} ion in octahedral symmetry is shown in Fig. 2. The free ion ground term of V^{3+} ($3d^2$) is ^3F and in an octahedral field this splits into $^3T_{1g}$ (strong-field limit = t_{2g}^2), $^3T_{2g}$ ($t_{2g}^1e_g^1$), and $^3A_{2g}$ (e_g^2) states in order of increasing transition energy. The ^3P free ion term transforms in O_h symmetry as another $^3T_{1g}$ state with a $t_{2g}^1e_g^1$ strong-field configuration, which mixes with the ground state via configuration interaction. The trigonal distortion in all of the compounds of interest splits the $^3T_{1g}$ ground state and the observable $^3T_{2g}$ and $^3T_{1g}$ excited states that give oriented single crystals a strong green-blue dichroism under polarized light in accordance with electric dipole selection rules for V^{3+} in a trigonal site symmetry (see Table 1) [14].

For less than half filled d orbitals, like for V^{3+}, one can also observe intra-configurational spin-forbidden transitions that have similar geometries in the ground and excited states. According to the Tanabe–Sugano diagram there are 3 such transitions that can be easily identified by their negligible dependence on $10Dq$ (slope ≈ 0). The expected line width (full-width at half-maximum, fwhm) of these spin-forbidden transitions is of the order of 1–10 cm^{-1} in contrast to spin-allowed electronic transitions that involve promotion of an electron into the anti-bonding e_g orbital and are expected to be orders of magnitude broader (see Fig. 2b). The experimentally observed line width of these intra-configurational spin-forbidden transitions in crystalline compounds is indeed of the order of 1 cm^{-1} in tris-oxalate, Al_2O_3, and hexa-urea lattices [2,4,14,15].

2.1. Trigonal distortions of $V^{III}O_6$ and $V^{III}(\bar{O}O)_3$ compounds

The reduction from octahedral symmetry by a trigonal distortion only splits T states, in contrast to tetragonal distortions that also split E states. Several similar parameterization schemes have been used to construct the matrix elements of the trigonal ligand field operator, $\mathcal{H}_{D_3}$ [18]. Following König and Kremer [19], the relation between Tanabe and Sugano's trigonal ligand field parameters K and K' for the diagonal and off-diagonal matrix elements, respectively [20], and v and v' introduced by Pryce and Runciman [8] are related by

$$\begin{aligned}
&\langle e_\pm(t_{2g})|\mathcal{H}_3|e_\pm(t_{2g})\rangle = \frac{1}{3}v = K,\\
&\langle a_1(t_{2g})|\mathcal{H}_{D_3}|a_1(t_{2g})\rangle = \frac{2}{3}v = 2K,\\
&\langle e_\pm(t_{2g})|\mathcal{H}_{D_3}|e_\pm(e_g)\rangle = v' = K'.
\end{aligned} \tag{2}$$

The other popular parameterization scheme by Ballhausen [18] and Liehr [21] employ $D\sigma$ and $D\tau$, which also redefines the octahedral ligand field parameter, Dq. The relations between those given in Eq. (2) are related to Ballhausen and Liehr's parameters by [19]:

$$\begin{aligned}
&Dq + \frac{7}{13}D\tau = Dq',\\
&\frac{1}{3}(9D\sigma + 20D\tau) = v = 3K,\\
&\frac{\sqrt{2}}{3}(3D\sigma - 5D\tau) = v' = K'.
\end{aligned} \tag{3}$$

The sign and magnitude of these trigonal ligand field components can be estimated if the trigonal splittings of the $^3T_{1g}$ ground and $^3T_{1g,2g}$ excited states are known using the simple relationships introduced initially by Macfarlane [9] and Rahman and Runciman [22]:

$$\begin{aligned}
&\Delta(^3T_{1g}(F)) = {}^3E{}^3A_2 \approx v + \frac{2}{3}v',\\
&\Delta(^3T_{2g}(F)) = {}^3E - {}^3A_1 \approx 0.461v + 0.0575v',\\
&\Delta(^3T_{1g}(P)) = {}^3E - {}^3A_2 \approx 0.54v - 0.45v'.
\end{aligned} \tag{4}$$

Eq. (4) shows that the off-diagonal trigonal matrix elements, v' or K', coupling the e orbitals cannot be neglected as was done in early studies [1,7] due to the fact that six-coordinate oxygen ligation results in an intermediate ligand field [9]. Pontnau and Adde [23] revised the relationships for the spin-allowed transitions slightly to give

$$\begin{aligned}
&\Delta(^3T_{1g}(F)) \approx -0.0392Dq + 0.119B + 0.986v + 0.615v',\\
&\Delta(^3T_{2g}(F)) \approx -0.0039Dq + 0.0324B + 0.449v + 0.027v',\\
&\Delta(^3T_{1g}(P)) \approx 0.036Dq - 0.155B + 0.562v - 0.605v'.
\end{aligned} \tag{5}$$

Macfarlane's treatment of V^{3+}:Al_2O_3 including the off-diagonal trigonal ligand field parameter provided spectroscopists with a framework for analyzing and accounting for differences in the sign of the excited state splittings between different $V^{III}O_6$ compounds (*vide infra*) [2,9].

The energies of the spin-forbidden transitions are the only transitions sensitive to the Racah C parameter [24]. It has been shown both theoretically [25] and experimentally [26] that the reduction of C and B are not equal and one would expect that the reduction in C is greater than B in coordination compounds due to covalency effects. Therefore fixing the nephelauxetic ratios of B and C to the same value often leads to unnecessary deviations between calculated and experimental ligand field energies and should be avoided whenever possible.

Computational tools, such as AOMX [27] and LigField [28] in combination with MagProp [29], now allow for experimental energies and crystallographically determined Euler angles (see Fig. 1) to be fit to the full ligand field within the framework of the angular overlap model. The ligand field parameters are replaced by angular overlap parameters that can be rationalized in terms of probable bonding interactions in the complex. A nice example that cannot be explained by ligand field theory is the origin of the large and positive trigonal field of the $[V(OH_2)_6]^{3+}$ complex in the β-alum structure by Tregenna-Piggott and co-workers [4]. The origin of the large trigonal field is a large anisotropy of the in-plane ($e_{\pi\|} \approx 0$) and out-of-plane ($e_{\pi\perp} \gg 0$) π-bonding parameters. The magnitude of this anisotropic π-bonding motif and thus the trigonal splitting of the $^3T_{1g}$ ground state is sensitive to changes in the orientation of water coordination as evidenced in the α and β modifications of the alum structure that will be discussed in Section 3 [30]. The extensive studies by Tregenna-Piggott and co-workers on the $[V(OH_2)_6]^{3+}$ complex in the solid state have demonstrated the efficacy of the angular overlap model in elucidating and rationalizing key magneto-structural correlations in transition metal compounds [3–5,30–32].

The large parameter space describing the full electronic structure of transition metal ions such as V^{3+} is often too cumbersome and unnecessary when we are interested in rationalizing the magnetic properties of the $V^{III}O_6$ and $V^{III}(\bar{O}O)_3$ complexes. Therefore, it is useful to neglect the mixing of the excited states with the $^3T_{1g}$ ground state (i.e., $10Dq \gg B$ or strong-field limit). In the next section, we describe two useful schemes for parameterizing the ZFSs of the $^3T_{1g}$ ground state, but we start with a set of angular overlap calculations in order to expose some aspects of the electronic structure that are not readily apparent in "simpler" parameterization schemes.

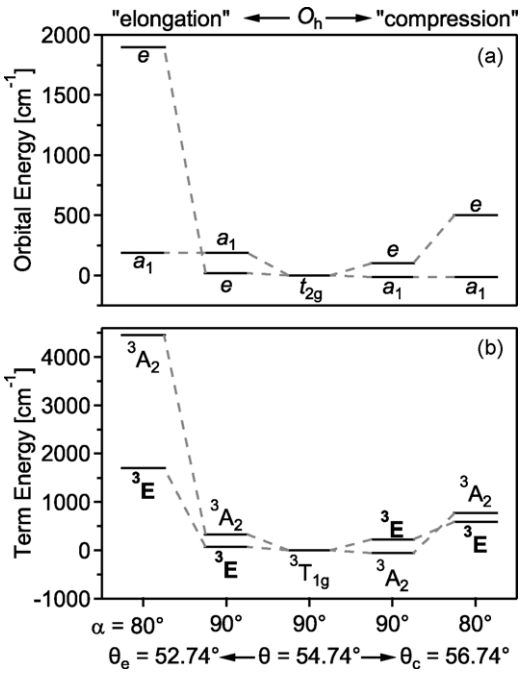

Fig. 3. Splitting diagram of (a) the t_{2g} orbitals and (b) the $^3T_{1g}$ ground state of a model $V^{III}(\bar{O}\bar{O})_3$ complex by elongation (to the left) and compression (to the right) along the D_3 axis of an octahedron by 2°. The effect of an additional reduction of the bite angle from $\alpha = 90°$ to 80° was also calculated. When $\alpha = 90°$ the first coordination sphere is similar to V^{3+}:Al_2O_3 or V(acac)$_3$; when $\alpha = 80°$ the coordination geometry is similar to $[V(ox)_3]^{3-}$. The φ and ψ Euler angles were determined assuming a planar bidentate ligand and Eqs. (6) and (7). Calculations were performed with no phase coupling and the following AOM parameters: $e_\sigma = 6667\,cm^{-1}$, $e_{\pi||} = e_{\pi\perp} = 500\,cm^{-1}$, $B = 550\,cm^{-1}$ and $C = 3000\,cm^{-1}$.

2.2. The $^3T_{1g}$ ground state and zero-field splittings

There are numerous studies devoted to the treatment of the axial splitting of the $^3T_{1g}$ ground state and ZFSs using various degrees of ligand field theory. The common distortion in mono-dentate $V^{III}O_6$ and $V^{III}(\bar{O}\bar{O})_3$ complexes is a compression along the three-fold molecular axis as in the β-alums [4] and $NaMgAl(ox)_3{\cdot}9H_2O$ [33]. However, caution must be taken when considering orbital and state splittings, especially with bidentate ligands such as in $V^{III}(\bar{O}\bar{O})_3$. Fig. 3 shows the orbital and state energies for a model $V^{III}(\bar{O}\bar{O})_3$ complex under different trigonal distortions from octahedral geometry in the absence of the Orgel effect [34,35] and spin–orbit coupling. The parameter for the octahedral ligand field of this model complex is taken as $10Dq = 18{,}000\,cm^{-1}$ and the Racah parameters are set to $B = 550\,cm^{-1}$ and $C = 3000\,cm^{-1}$. The calculations were performed using the angular overlap model (AOM) implemented in the AOMX program package [27] with the restrictions on the φ and ψ Euler angles defined for planar bidentate ligands shown in Fig. 1 given by Atanasov et al. [34]:

$$\varphi = 2\cos^{-1}\left[\frac{\cos(\alpha/2)}{\sin\theta}\right], \tag{6}$$

$$\psi = \cos^{-1}\left[\frac{\cos\theta\cdot\cos(\varphi/2)}{\sin(\alpha/2)}\right]. \tag{7}$$

Under a trigonal distortion the t_{2g} orbital splits into an orbital singlet (a_1) and an orbital doublet (e) as shown in Fig. 3a. Keeping the bite angle α fixed at 90°, a trigonal compression (θ_c) destabilizes the orbital doublet and thus $a_1 < e$ [27,36]. The opposite scenario is observed for a trigonal elongation (θ_e). When we allow for the bite angle to change, for instance from a six-membered chelate ring with acac coordination, $\alpha \approx 88°$ [37], to a six-membered chelate ring with ox coordination, $\alpha \approx 80°$ [36,38], the orbital splittings change significantly. In both cases the e orbital is destabilized by many hundreds of cm^{-1} by a reduction in the twist angle φ, which results in a change in the ordering for a trigonal elongation. This situation changes somewhat when we consider the term representations that arise from placing two electrons into the orbitals as shown in Fig. 3b. If we neglect configuration interaction and assume the strong-field t_{2g}^2 configuration, then the irreducible representations of the states are simply the direct product of the electronic configurations: $e^1 \times e^1 = {}^3A_2$ and $a_1^1 \times e^1 = {}^3E$. However, we are not in the strong-field limit with oxo-coordination and we must consider electron–electron repulsion explicitly for the d^2 electronic configuration. The calculated state energies shown in Fig. 3b demonstrate the importance of including configuration interaction and electron–electron repulsion in the treatment of many-electron systems, especially when the differences in orbital energies are small such as the cases when $\alpha = 90°$. The AOM calculations show that the sign and magnitude of the axial splitting for both trigonal elongations and compressions of an octahedron can be greatly influenced by the reduction of the bite angle for tris-bidentate coordination.

The magnetic anisotropy of pseudo-octahedral V^{3+} complexes is determined by the sign and magnitude of the ZFS of the $^3T_{1g}$ ground state. For recent reviews focusing on the ZFS of different transition metal ions in coordination compounds, including V^{3+} complexes, see [39–41]. Early studies of the magnetic susceptibility of V^{3+} compounds simplified the Hamiltonian in Eq. (1) to consider only the $^3T_{1g}$ multiplet [42,43]. This simpler Hamiltonian operates within the "fictitious" $L = 1$ and $S = 1$ basis functions according to Abragam and Pryce [10,44] and is given by

$$\mathcal{H}' = \Delta_{ax}[\hat{L}_z^2 - \frac{1}{3}L(L+1)] + \Delta_{rh}[\hat{L}_x^2 - \hat{L}_y^2] - A\lambda(\mathbf{L}\cdot\mathbf{S}), \tag{8}$$

where Δ_{ax} and Δ_{rh} are effective splitting parameters that absorb the effects of the trigonal and rhombic orbital splittings and electronic repulsion [10,44]. The reason for including the Δ_{rh} splitting parameter is due to the recent experimental evidence of large rhombic distortions of the $[V(urea)_6]^{3+}$, V(acac)$_3$, and $[V(ox)_3]^{3-}$ complexes in the solid state [14,36,45]. The full 9×9 matrix is given in Ref. [14]. The last term takes into account configuration interaction with the upper $^3T_{1g}$ state from the ^3P free ion term by the parameter A [10]. This parameter takes a value between 1.5 (weak-field limit) and 1.0 (strong-field limit). In hexa-oxo-coordination the ligand field strength is intermediate and takes on the value of $A \approx 1.25$ [42]. The spin–orbit coupling coefficient has a free ion value of $\zeta/2S = \zeta/2 = \lambda = 105\,cm^{-1}$ [46], and is expected to be reduced in the complex due the nephelauxetic and possible Ham effects. The calculation of the g-values is possible with an external magnetic field by adding the Zeeman operator, $(k\boldsymbol{L}+2\boldsymbol{S})\mu_B\mathbf{B}$, to Eq. (8). The theoretical anisotropy of the g-values will be $g_z > g_x \sim g_y$ when $\Delta_{ax} \gg A\lambda \gg |\Delta_{rh}|$ [40], which is in agreement with experimental observations [5,16,45].

For the majority of pseudo-octahedral V^{3+} oxo compounds studied to date, the anisotropic ligand field produces a large and positive axial splitting compared to the magnitude of the spin–orbit coupling. In this scenario the resulting ground state in trigonal symmetry is $^3A_2$, which is further split by spin–orbit coupling into a spin singlet, $M_S = |0\rangle = A_1$, and spin doublet, $M_S = (1/\sqrt{2})(|1\rangle \pm |-1\rangle) = E$ with typical splittings of 3–10 cm^{-1}. Under the scenario that $\Delta_{ax} \gg A\lambda \gg |\Delta_{rh}|$ the influence of the upper ^3E state can be neglected and the splitting of the $^3A_2$ ground term can be parameterized using axial and rhombic ZFS parameters, D and E. These parameters are defined by the axial $S = 1$ spin-Hamiltonian given by

$$\mathcal{H}_{S=1} = D[\hat{S}_z^2 - \frac{1}{3}S(S+1)] + E[\hat{S}_x^2 - \hat{S}_y^2] + \mathbf{g}\mu_B\mathbf{B}, \tag{9}$$

where $\mathbf{g}$ is the Landé $\mathbf{g}$-tensor, μ_B is the Bohr magneton, and $\mathbf{B}$ is the strength of an external magnetic field. The study of non-Kramers

ground states has seen much more attention recently due to the development and availability of high-frequency and high-magnetic field electron paramagnetic resonance (HFEPR) spectroscopy that can bridge large axial ZFS energies of pseudo-octahedral V^{3+} compounds [5,36,39,45]. The interested reader is referred to the following reviews on the use of HFEPR as a sensitive probe of the ZFS and principal *g*-values of coordination compounds [39]. When $\Delta_{ax} \gg A\lambda \gg |\Delta_{rh}|$, the ZFS parameters derived by second-order perturbation theory [3,14] are

$$D \approx \frac{(A\lambda)^2}{\Delta_{ax}}, \quad |E| \approx \left(\frac{|\Delta_{rh}|}{\Delta_{ax}}\right) D, \quad \text{and} \quad \frac{|E|}{D} \approx \frac{|\Delta_{rh}|}{\Delta_{ax}} \leq \frac{1}{3}. \tag{10}$$

A more thorough treatment of these perturbation expressions including contributions from the Jahn–Teller effect of the ^3E state are beyond the scope of this review and the interested reader is referred to the theoretical paper by Tregenna-Piggott and Carver [3].

In contrast to the overwhelming consensus in the literature that the axial ZFS parameter is positive for $V^{III}O_6$ and $V^{III}(\ddot{O}\ddot{O})_3$ compounds, we recently discovered that the $[V(ox)_3]^{3-}$ anion can have both positive *and* negative values depending on the particular host lattice [14]. However, the above scenario with $\Delta_{ax} \gg A\lambda \gg |\Delta_{rh}|$ does *not* allow for the possibility of negative *D* values according to Eq. (10). Again starting from the Hamiltonian given in Eq. (8), it was shown that the only scenario that yields a negative value for *D* was with a large and negative Δ_{ax} followed by an appreciable Δ_{rh} in order to split the ^3E ground state into separated orbital singlets (i.e., $|\Delta_{ax}| \gg |\Delta_{rh}| \gg A\lambda$). This scenario results in a ^3A ground state (C_1 notation) whose energy splittings can be modeled using the axial $S = 1$ spin-Hamiltonian of Eq. (9). The expressions derived by perturbation theory when $\Delta_{ax} \ll 0$ and $|\Delta_{ax}| \gg |\Delta_{rh}| \gg A\lambda$ are given by

$$D \approx \frac{\Delta_{ax}}{|\Delta_{rh}|}|E| < 0, \quad |E| \approx \frac{(A\lambda)^2}{2(|\Delta_{rh}| - \Delta_{ax})} \quad \text{and} \quad \frac{|E|}{|D|} \approx \frac{|\Delta_{rh}|}{|\Delta_{ax}|} \leq \frac{1}{3}. \tag{11}$$

In Eq. (11) the value of *D* is always negative under these constraints since Δ_{ax} is negative. The 1/3 restriction in Eqs. (10) and (11) is phenomenological and simply keeps the rhombic component quantized perpendicular to the axial splitting and small. When the ratio of $|E|/|D|$ is exactly 1/3, then there are two equivalent set of parameters; one with Δ_{ax} having a positive value and another having a negative value.

Figure 4 summarizes graphically the splitting of the $^3T_{1g}$ ground state by the various splitting parameters with constant $A\lambda = 100\,cm^{-1}$. In Fig. 4a, at $\Delta_{ax} = 0$ the $^3T_{1g}$ state splits into *J* sub-levels with $J = 2 < 1 < 0$. The grouping of the states into an orbital singlet and doublet only occurs with large $|\Delta_{ax}|$ values. Fig. 4b shows the dependence of the spin–orbit states (spinors) when $\Delta_{ax} = \pm 1500\,cm^{-1}$ as a function of an addtional rhombic splitting, $|\Delta_{rh}|$. The vertical dashed line at $|\Delta_{rh}| = 500\,cm^{-1}$ is when the $|\Delta_{rh}|/|\Delta_{ax}|$ ratio is exactly 1/3, yielding the scenario where the energies of the spinors are equal for $\Delta_{ax} = +1500\,cm^{-1}$ and $\Delta_{ax} = -1500\,cm^{-1}$. By considering only the lowest ^3A state and subtracting the lowest energy spinor we can obtain Fig. 4c from the data presented in Fig. 4b. The solid lines give the physically possible scenarios due to the restriction that $|\Delta_{rh}|/|\Delta_{ax}| \leq 1/3$. It is clear from Fig. 4c that the only scenario for having a positive (negative) axial ZFS spin-Hamiltonian parameter is by starting with a large positive (negative) Δ_{ax} splitting parameter. The perturbation expressions given by Eqs. (10) and (11) are given by dashed-dotted lines for the different scenarios. The energies of the different excited states and their relation to the spin-Hamiltonian parameters are given in Fig. 4c.

Rhombic distortions result in an anisotropy of the *g*-values along the principal axes for both Kramers and non-Kramers ions

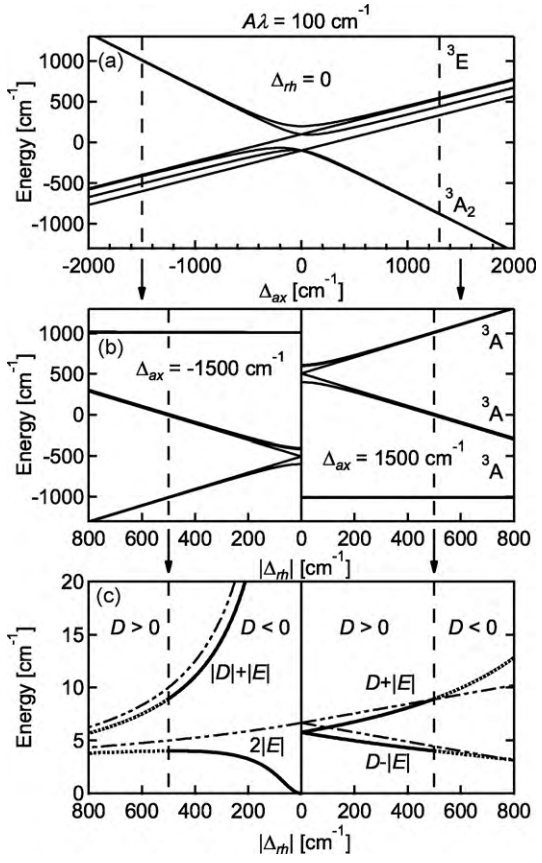

Fig. 4. (a) Calculated splitting of the $^3T_{1g}$ ground state as a function of positive and negative Δ_{ax} with $A\lambda = 100\,cm^{-1}$ and $\Delta_{rh} = 0$. At $\Delta_{ax} = 0$, the $^3T_{1g}$ ground state splits into pure *J* sub-levels with an ordering of $J = 2 < 1 < 0$. With increasing $|\Delta_{ax}|$, the nine spinors group into $^3A_2$ and ^3E states. (b) Calculated effect of non-zero $|\Delta_{rh}|$ splitting with $A\lambda = 100\,cm^{-1}$ and $\Delta_{ax} = -1500\,cm^{-1}$ (left panel) and $+1500\,cm^{-1}$ (right panel). Increasing the $|\Delta_{rh}|$ parameter removes the orbital degeneracy of the ^3E state and in C_1 symmetry there are three separated ^3A terms. The magnetic properties are largely determined by the energy separation of the three lowest lying spin–orbit levels (spinors) of the ^3A ground state. The dashed vertical line is where $|\Delta_{rh}|/|\Delta_{ax}| = 1/3$ ($|\Delta_{rh}| = 500\,cm^{-1}$ in this case). The energies of all spinors at this ratio are equivalent for positive and negative Δ_{ax} values. (c) Energies of the two lowest excited spinors with respect to the ground state spinor composing the lowest ^3A state in (b). The axial ZFS parameter, *D*, can be determined using the $S = 1$ spin-Hamiltonian. It follows in (c) that the sign of Δ_{ax} is correlated to the sign of *D* as long as $|\Delta_{rh}|/|\Delta_{ax}| \leq 1/3$ shown by the dashed vertical line. When $|\Delta_{rh}|/|\Delta_{ax}|$ increases to greater than 1/3, the signs of *D* and Δ_{ax} change since the lowest energy separation defined as $2|E|$ changes and is shown as dotted lines. The calculated spinor energies using the perturbation expressions given in Eqs. (10) (right panel) and (11) (left panel) are shown in (c) with dashed-dotted lines.

(i.e., $g_{xx} \neq g_{yy} \neq g_{zz}$). However, for non-Kramers ions such as V^{3+} with unquenched orbital angular momentum the rhombic field also removes the orbital degeneracy which manifests itself by an additional splitting of the spin–orbit states. This unique feature of non-Kramers ions allows for the possibility to resolve rhombic components to the ZFS optically in the absence of a magnetic field. Such spectral features have been resolved in the high-resolution absorption spectroscopy of $[V(ox)_3]^{3-}$ complexes in the solid state and are discussed in the next section.

3. Case studies: spectroscopic investigations of $V^{III}O_6$ and $V^{III}(\ddot{O}\ddot{O})_3$ complexes

3.1. Electronic absorption spectroscopy

The electronic absorption spectroscopy of $V^{III}O_6$ and $V^{III}(\ddot{O}\ddot{O})_3$ complexes in the solid state has initially been limited to determining the energies of the spin-allowed transitions and their

polarization and temperature dependence [1,2,4,7]. Fig. 5 shows the electronic absorption spectra of V^{3+} in Al_2O_3 at 77 K [1], in $Rb[V(OH_2)_6](SO_4)_2{\cdot}6H_2O$ at 16 K [4], in $[V(urea)_6](ClO_4)_3$ at 77 K [2], and doped into $NaMgAl(ox)_3{\cdot}9H_2O$ at 77 K [7]. From Fig. 5, we immediately see that the polarization dependence of the visible $^3A_2(^3T_{1g}) \rightarrow {}^3\Gamma(^3T_{1g})$ spin-allowed transition is the complete opposite for V^{3+}:Al_2O_3 compared to $[V(urea)_6](ClO_4)_3$ and the $[V(ox)_3]^{3-}$ compounds. Although the Al^{3+} site in Al_2O_3 has C_3 symmetry only, it is very close to C_{3v} and spectroscopic transitions of impurity ions may be treated in this higher symmetry [1]. Thus in V^{3+}:Al_2O_3 the $^3A_2(^3T_{1g}) \rightarrow {}^3A_1(^3T_{1g})$ transition is therefore forbidden with π-polarized light according to the electric dipole selection rules for D_3, C_{3v} and C_3 molecular symmetries given in Table 1. McClure calculated the relative electric dipole strengths for the one-electron spin-allowed excitations for a d^2 ion in C_{3v} symmetry for both $^3A_2$ and ^3E trigonal components of the $^3T_{1g}$ ground state [1]. The polarized absorption shown in Fig. 5a of V^{3+}:Al_2O_3 has only a slight deviation between the calculated and experimental intensities for a $^3A_2$ ground state in a rigorously trigonal site symmetry [1]. In simpler terms, the main source of band intensity in the case of V^{3+}:Al_2O_3 is due to the lack of inversion symmetry. Therefore the difference observed in the other lattices must come from an alternative intensity gaining mechanism for instance due to the admixture of ^3E character into the ground state through a rhombic crystal field. Despite crystallizing in the same space group as α-Al_2O_3, the $[V(urea)_6](ClO_4)_3$ compound has an appreciable rhombic component to the ZFS of $|E| = 0.573\ cm^{-1}$ ($E/D \approx 0.1$) that was observed by HFEPR and magnetic susceptibility (*vide infra*) [36]. In the tris-oxalate lattices the rhombic distortion is even more pronounced [14,15]. These deviations from trigonal site symmetry are likely responsible for the inversion of the polarization intensities of the $^3A_2$ and ^3E trigonal components of the $^3T_{1g}$(P) state among the lattices shown in Fig. 5.

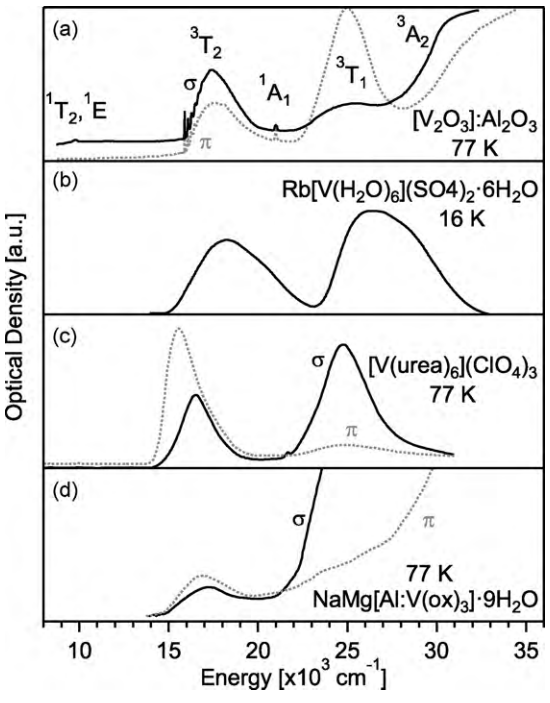

Fig. 5. Single crystal electronic absorption spectra of V^{3+} in various crystalline lattices collected at low temperature. See individual panels for lattices and temperatures. The solid lines are σ-polarized spectra and the dotted lines are π-polarized spectra in parts (a), (c), and (d). The spectrum of $Rb[V(H_2O)_6](SO_4)_2{\cdot}6H_2O$ shown in (b) is unpolarized. Spectra were digitized using a commercial program (DigitizeIt 1.5.7, http://www.digitizeit.de) from Refs. [1,30,2,7], respectively. Spectra in (a) are offset for clarity.

As discussed in Section 2.2 and shown in Fig. 3, one would expect the ground state in an idealized $[V(ox)_3]^{3-}$ complex with D_3 symmetry to be the ^3E trigonal component of the $^3T_{1g}$ state as a result of the acute V(ox) bite angle. The inversion of the polarization intensities compared to V^{3+}:Al_2O_3 is thus not surprising. However, inspection of the crystal structures for the $[V(ox)_3]^{3-}$ salts reveals only C_1 molecular symmetry of the V^{3+} ion [33,38] and the bands should not exhibit a polarization dependence. It can thus be concluded that the tris-bidentate coordination provides a well-defined D_3 parent pseudo-symmetry that manifests itself in a strong polarization of the spin-allowed bands shown in Fig. 5 [14,15].

Dingle et al. pointed out a possible difference in the sign of the $^3T_{2g}$ trigonal splitting between V^{3+}:Al_2O_3 and $[V(urea)_6](ClO_4)_3$ [2]. The authors tentatively attributed this observation to a change in the sign of the off-diagonal trigonal ligand field parameter as a result of their analysis using Macfarlane's equations to quantify v and v' discussed above [9]. The argument was tentative due to the small splitting in the low-temperature electronic absorption spectra of V^{3+}:Al_2O_3. This transition also displays a vibronic progression in both polarizations with intervals of ~200 cm^{-1} with similar intensities and corresponding to an *e* vibration. This is a clear indication of a dynamic JT effect and has been the focus of many studies [47]. Accurate assignment of the transition energies in the π- and σ-polarized spectra of V^{3+}:Al_2O_3 is difficult and thus it is reasonable to assume that the reported trigonal $^3T_{2g}$ splitting of −70 cm^{-1} by McClure is within the error of the analysis [1].

High-resolution electronic absorption spectroscopy of the intra-configurational spin-forbidden $^3T_{1g} \rightarrow {}^1E(^1T_{2g})$ and $^1A_1(^1A_{1g})$ transitions of $V^{III}O_6$ and $V^{III}(\bar{O}\bar{O})_3$ in crystalline environments at cryogenic temperatures have comparatively narrow inhomogeneous line widths, Γ_{inh}, as expected from Fig. 2b. Fig. 6 shows the high-resolution spectra of the $^3A_2(^3T_{1g}) \rightarrow {}^1E(^1T_{2g})$ transition of a 0.8% V^{3+}:Al_2O_3 crystal in the near-infrared region at 4.2 K. The spectra were collected using a high-resolution Fourier-transform (FT) spectrometer with spectral resolutions ranging from 10 to 0.5 cm^{-1} as described elsewhere [14,15]. At the lowest resolution (10 cm^{-1}) the transition appears as a single, broad and asymmetric band. At 4.0 cm^{-1} resolution it increases in intensity and a shoulder is revealed at higher energy. The latter becomes clearly resolved at spectral resolution better than 2.0 cm^{-1}. At 0.5 cm^{-1} resolution there are two clearly resolved bands with an energy splitting of

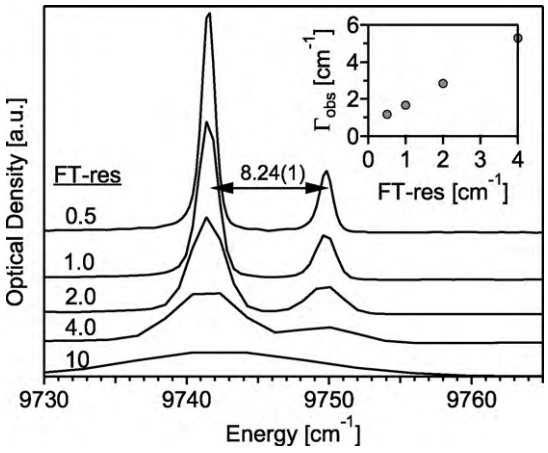

Fig. 6. Unpolarized Fourier-transform (FT) electronic absorption spectrum of V^{3+}:Al_2O_3 (0.8% V_2O_3) as a function of the instrument resolution (FT-res) at 4.2 K. Inset: Average observed line width (Γ_{obs}) as a function of the FT-res determined by fitting the absorption features with two Voigt band shapes with constant energy splitting of 8.24 cm^{-1}. There is a clear decrease in Γ_{obs} with decreasing FT-res demonstrating these bands are still instrument-limited even at 0.5 cm^{-1}.

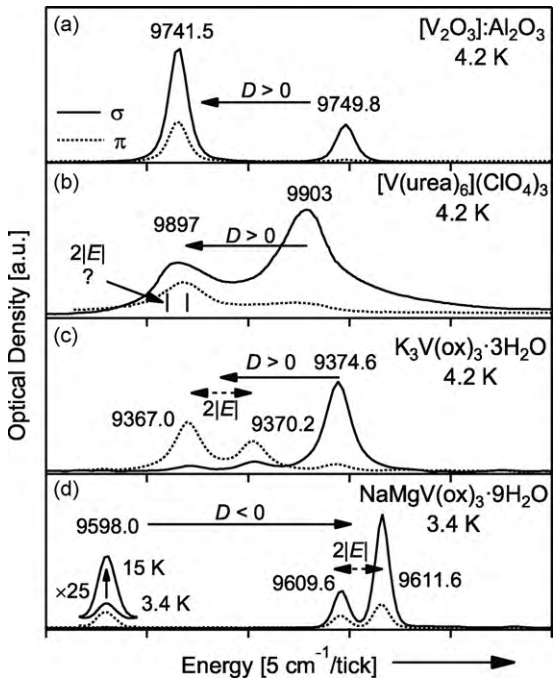

Fig. 7. Polarized electronic absorption spectra of the $^3T_{1g} \rightarrow {}^1T_{2g}$ transition (O_h notation) of (a) V^{3+}:Al_2O_3 (0.8% V_2O_3) at 4.2 K [50], (b) $[V(urea)_6](ClO_4)_3$ at 4.2 K [2], (c) $K_3V(ox)_3{\cdot}3H_2O$ (Site "A") at 4.2 K [14], and (d) $NaMgV(ox)_3{\cdot}9H_2O$ at 3.4 and 15 K [14]. The *x*-axis spans 25 cm^{-1}, and the energies of the individual transitions are given in the figure next to the peak. The solid horizontal lines denote the axial ZFS parameter, *D*, and its sign among the different lattices. For the $[V(ox)_3]^{3-}$ salts in (c) and (d), the rhombic ZFS is shown with a double-headed arrow with a dashed line. Spectra in (b) were digitized from ref. [2].

8.24(1) cm^{-1}. The inset shows the decrease in the observed line width with better spectral resolution [48]. Even at the best spectral resolution, the observed line width is limited by the spectrometer, that is the inhomogeneous line width $\Gamma_{inh} < 1.0\,cm^{-1}$. The same energy splitting of ~8.3 cm^{-1} has also been observed for the spin-flip transition in the visible, $^3A_2(^3T_{1g}) \rightarrow {}^1A_1({}^1T_{2g})$, which can therefore only be the result of an axial ZFS of the $^3A_2$ ground state by spin–orbit coupling [8,16,17,49].

Fig. 7 shows the single crystal polarized $^3\Gamma(^3T_{1g}) \rightarrow {}^1E({}^1T_{2g})$ absorption of V^{3+}:Al_2O_3 [50], $[V(urea)_6](ClO_4)_3$ [2], $K_3V(ox)_3{\cdot}3H_2O$ [14], and $NaMgV(ox)_3{\cdot}9H_2O$ [14]. The polarized spectra of V^{3+}:Al_2O_3 have been recollected on the same crystal shown in Fig. 6. The splittings observed in the electronic absorption spectra of the compounds in Fig. 7 are the result of the ZFS of the $^3T_{1g}$ ground state. The spin-Hamiltonian of Eq. (9) outlines the priority in assigning the spin-Hamiltonian parameters, *D* and *E*, to the resolved splittings with the smallest energy separation assigned to $2|E|$. In the case of V^{3+}:Al_2O_3 this is not possible since $E = 0$, therefore we must rely on the polarization or magnetic field dependence of the lines to assign the doubly-degenerate spinor experimentally [8,16,17]. Based on the arguments in Section 2 and the calculated splitting behavior of the $^3T_{1g}$ ground state shown in Fig. 3, the scenario where the 8.3 cm^{-1} splitting originates from a ^3E ground state without a rhombic contribution can be eliminated from consideration. A similar situation is found for $[V(urea)_6](ClO_4)_3$ with the exception that Beaulac et al. reported a rhombic splitting of $|E| = 0.573\,cm^{-1}$ from HFEPR [36]. This corresponds to an expected splitting of the lowest energy feature shown in Fig. 7b by ~1.15 cm^{-1}. With this recent observation of a small rhombic component to the ZFS, the high-resolution polarized absorption spectra collected by Dingle et al. could be reinterpreted to exhibit such a rhombic splitting by close inspection of the position and asymmetry of the lowest energy line collected in π and σ polarizations (see vertical bars separated by 1.15 cm^{-1} in Fig. 7b).

The polarized absorption spectra of the spin-forbidden near-IR transition of the $[V(ox)_3]^{3-}$ complex in two lattices shown in Fig. 7c and d clearly exhibit an additional splitting that originates from a large rhombic component to the ZFS [14,15]. The smallest splitting of the $^3T_{1g}$ ground state from spectral deconvolution of the spin-forbidden bands in the neat $NaMgV(ox)_3{\cdot}9H_2O$ lattice is $2|E| \approx 2\,cm^{-1}$ and 3 cm^{-1} for the mixed crystal $NaMg[Al_{1-x}V_x(ox)_3]{\cdot}9H_2O$ with $x = 0.013$ (spectra not shown) [14,15]. In the multi-site $K_3V(ox)_3{\cdot}3H_2O$ lattice the $2|E|$ values are in the range from 1.9 to 3.3 cm^{-1} [14]. However, the $2|E|$ splitting in the $NaMg[Al_{1-x}V_x(ox)_3]{\cdot}9H_2O$ systems occurs between the two lines at highest energy whereas in $K_3V(ox)_3{\cdot}3H_2O$ and $Na_3V(ox)_3{\cdot}5H_2O$ (spectra not shown) is between the two lines at lowest energy (see Fig. 7c and d) [14]. This requires the sign of the axial ZFS parameter, *D*, to be positive for $[V(ox)_3]^{3-}$ in $K_3V(ox)_3{\cdot}3H_2O$ (and $Na_3V(ox)_3{\cdot}5H_2O$) and negative for $NaMg[Al_{1-x}V_x(ox)_3]{\cdot}9H_2O$ [14].

In the various tris-oxalate lattices the inhomogeneous line width, Γ_{inh}, of the $^3\Gamma(^3T_{1g}) \rightarrow {}^1\Gamma({}^1T_{2g})$ transitions is generally somewhat larger than in V^{3+}:Al_2O_3, but can be resolved with the FT spectrometer. With $\Gamma_{inh} = 0.86(3)\,cm^{-1}$, it is smallest for neat $[NaMgV(ox)_3]{\cdot}9H_2O$ [14,50]. Even in $K_3V(ox)_3{\cdot}3H_2O$, a lattice with a low-temperature crystallographic phase transition and multiple sites, the average Γ_{inh} of the transitions in Fig. 7c is only 1.4(2) cm^{-1} [14]. We have also studied Γ_{inh} of the $^3A(^3T_{1g}) \rightarrow {}^1E({}^1T_{2g})$ and $^3A(^3T_{1g}) \rightarrow {}^1A_1({}^1A_{1g})$ transitions for the series of $NaMg[Al_{1-x}V_x(ox)_3]{\cdot}9H_2O$ crystals with varying *x* values from 0.013 to 1 and present the observed trend in Fig. 8 [14,15]. The contribution to Γ_{inh} by inhomogeneous ligand fields is expected to be minimized at the two extremes ($x = 0.013$ and 1) where the corresponding values are ~0.9 cm^{-1} and ~1.4 cm^{-1} for the $^1E(^1T_{2g})$ and $^1A_1(^1A_{1g})$ electronic origins in $NaMgV(ox)_3{\cdot}9H_2O$, respectively. The energy of the $^1A_{1g}$ state has a non-vanishing dependence on 10*Dq* that is identifiable by a slightly positive slope in the Tanabe–Sugano diagram shown in Fig. 2. In contrast the near-IR states originating from the ^1D free ion term show no dependence 10*Dq* whatsoever in O_h symmetry [14,24]. The larger experimental value of Γ_{inh} for the $^1A_1(^1A_{1g})$ transition for all concentrations shown in Fig. 8 confirms this expectation. The mismatch in ionic radii of ~20% between octahedral V^{3+} (64 pm) and Al^{3+} (53.5 pm) [51] creates large strains in the crystal field and is the main factor for the increase in Γ_{inh} with increasing *x* values of 0.083 and 0.15 in Fig. 8. An additional

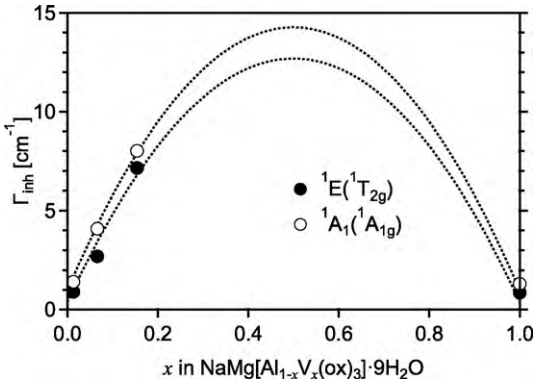

Fig. 8. Average inhomogeneous line widths of the $^3T_{1g} \rightarrow {}^1E({}^1T_{2g})$ (filled circles) and $^3T_{1g} \rightarrow {}^1A_1({}^1A_{1g})$ (open circles) spin-forbidden transitions of $NaMgAl_{1-x}V_x(ox)_3{\cdot}9H_2O$ when $x = 0.013$, 0.083, 0.15, and 1. The dashed line is a fit of data to $\Gamma_{inh} = \Gamma_{inh,max} + c(x - 0.5)^2$, where *c* is a variable defining the curvature of the parabola, and $\Gamma_{inh,max}$ is the Γ_{inh} value at its expected maximum value at $x = 0.5$. This fit estimates $\Gamma_{inh,max}$ values of ~12.7 cm^{-1} and ~14.3 cm^{-1} for the $^1E(^1T_{2g})$ and $^1A_1(^1A_{1g})$ transitions, respectively.

contribution to the line width from very rapid spin-lattice relaxation due to the large ZFSs may be significant even when $x = 0.013$ and 1.

Dingle et al. reported the polarized absorption of the $^3A_2(^3T_{1g}) \rightarrow {}^1A_1(^1A_{1g})$ transition of $[V(urea)_6](ClO_4)_3$ at 21638 cm^{-1}. However, in this case the larger value of Γ_{inh} of the transition from ligand field effects [24] did not allow for the axial ZFS to be resolved [2]. The reported temperature dependence of the $^1A_1$ line at 21638 cm^{-1} shown in Fig. 9b clearly indicates a large positive axial ZFS. Dingle et al. claim the maximum intensity of the transition is obtained at 20 K and in some cases with zero intensity at 1.5 K. The perchlorate and iodide compounds crystallize in the e_g^2 space group [2,52] with the V^{3+} center at a site with D_3 symmetry. The ground state of the $[V(urea)_6]^{3+}$ complex cation in the solid state is $^3A_2(^3T_{1g})$, which splits into A_1 and E spinors by spin–orbit coupling with the E spinor situated 6 cm^{-1} above the A_1 spinor [2,36]. Taking into account Boltzmann population statistics and the electric dipole selection rules given in Table 1, the observations by Dingle et al. are indeed valid for the $[V(urea)_6](ClO_4)_3$ compound with strict adherence to a D_3 site symmetry [2].

The electronic absorption spectra of the spin-forbidden transitions presented in Fig. 7 also display vibrational (vibronic) side bands. Fig. 9 shows the absorption spectra including the vibrational fine structure of the $^3A_g(^3T_{1g}) \rightarrow {}^1E_g(^1T_{2g})$ transition for $[V(OH)_6]^{3+}$, and the $^3\Gamma(^3T_{1g}) \rightarrow {}^1A_1(^1A_{1g})$ transition for $[V(urea)_6]^{3+}$ and $[V(ox)_3]^{3-}$ compounds. In the spectra of Fig. 9, the energy scale is given with respect to the respective electronic origin. The $[V(OH)_6]^{3+}$ complex in $Rb[V(OH_2)_6](SO_4)_2{\cdot}6H_2O$ has S_6 symmetry. Thus the intensity of the $^3A_g(^3T_{1g}) \rightarrow {}^1E_g(^1T_{2g})$ transition is only allowed by a magnetic dipole mechanism [30]. Tregenna-Piggott et al. also observed similar vibrational side bands coupled to the $^2E_g \rightarrow {}^4A_{2g}$ emission of $Cs[Cr(OH_2)_6](SO_4){\cdot}6H_2O$, which indicates the mechanism for coupling of vibrations to electronic origins is more dependent on the vibrational modes of the β-alums than on the identity of the transition metal ion [30]. In contrast to the β-alums there is no inversion symmetry of the chromophores in $[V(urea)_6](ClO_4)_3$ [2] or $NaMg[Al_{1-x}V_x(ox)_3]{\cdot}9H_2O$ ($x = 0.083$ [33]) and the majority of the intensity is concentrated in the electric dipole allowed origins. As a consequence the spectra have to be scaled in the region of the vibrational side bands in order to be observable in Fig. 9b and c. The vibrational side bands of the Cr^{3+} analogs of these two lattices have also been reported with similar structure to the V^{3+} compounds [53].

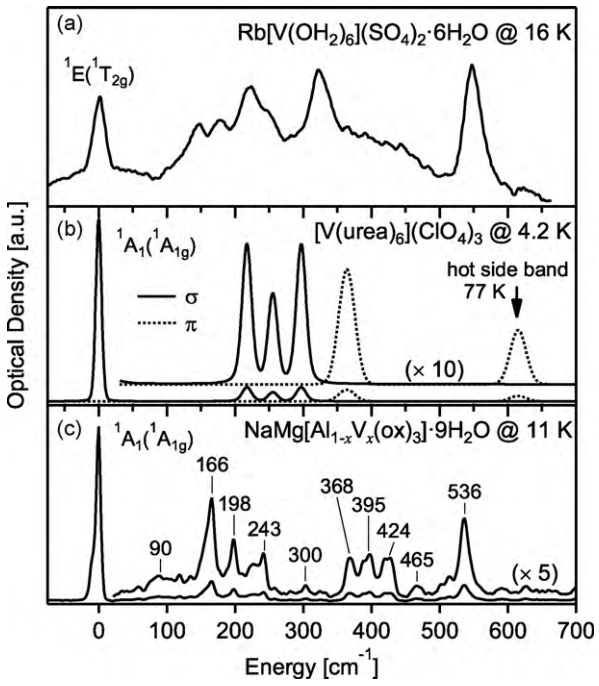

Fig. 9. Electronic absorption spectra at low temperature of the vibronic side bands of the $^1E(^1T_{2g})$ electronic origin of (a) $Rb[V(OH_2)_6](SO_4)_2{\cdot}6H_2O$ and the $^1A_1(^1A_{1g})$ electronic origins of (b) $[V(urea)_6](ClO_4)_3$ and (c) $NaMg[Al_{1-x}V_x(ox)_3]{\cdot}9H_2O$ ($x = 0.083$). The spectra in (a) and (b) were digitized from Refs. [30,2], respectively. The spectra in (b) was corrected for the overlapping $^3T_1(F) \rightarrow {}^3T_1(P)$ absorption. Polarized spectra are shown in (b). Energies of the side bands are given in (c). Temperatures are given in the figure.

Table 2 presents the reported assignments and energies of the ligand field states and ligand field parameters including the trigonal ligand field parameters expressed in terms of v and v'. The energies of the spin-forbidden and spin-allowed transitions and the calculated ligand field parameters for the various compounds reflect the large variability among the 1st coordination spheres of the oxo ligands reviewed. The energies of the spin-allowed transitions of octahedral V^{3+} depend on Dq and B, while the spin-forbidden transitions also have a dependence on the C Racah parameter. Therefore C cannot be estimated independently if no spin-forbidden transition is detected, which is the case for $V(acac)_3$. The octahedral splitting parameter, $10Dq$, follows the trend: $urea < ox^{2-} < O^{2-} < OH_2 < acac^-$. This trend is in agreement with the experimental trend across a vast majority of coordination compounds [46]. The B values provide a direct comparison of nephelauxetic ratios, $\beta = B/B_0$, among the lattices and a quantitative estimate of covalency trends between the ligands [46]. The B values order with $ox^{2-} < O^{2-} < OH_2 \sim urea < acac^-$; thus the most covalent $V^{III}O_6$ or $V^{III}(\bar{O}\bar{O})_3$ ligand field in Table 2 is estimated to be $[V(ox)_3]^{3-}$.

The variation in ligand fields among the lattices is exemplified by the ZFS values among the lattices in Table 2. In compounds with no rhombic component to the ZFS there is almost a 70% difference in the axial ZFS splitting of the $^3A_2$ ground state between the Al_2O_3 and hexa-aqua lattices [30,49]. From Eq. (9) it is clear that the reduction in D in the hexa-aqua lattice is due to ~80% increase in the Δ_{ax} value that has been confirmed experimentally (*vide infra*, see Table 2).

The ground state ZFS of the tris-bidentate complexes, $V(acac)_3$ and $[V(ox)_3]^{3-}$, exhibits a large contribution from rhombic distortions. In $V(acac)_3$, the rhombicity is the largest reported for any $V^{III}O_6$ or $V^{III}(\bar{O}\bar{O})_3$ compound with $E/D = 0.26$ [45]. Perhaps the most interesting complex as far as diversity of the electronic ground state is arguably that of $[V(ox)_3]^{3-}$ in different lattices [14,15]. The coordination environment in the $[V(ox)_3]^{3-}$ compounds is strongly perturbed by outer-shell or 2nd coordination sphere interactions through strong hydrogen bonding of free and/or bound crystalline water molecules to the oxalate ligands and crystal packing forces [14,15]. Crystalline disorder in the $K_3V(ox)_3{\cdot}3H_2O$ lattice also contributes to the anisotropic ligand field [38]. Fig. 10 shows the explicit packing motifs and H-bonding from the water molecules to the oxalate ligands in $NaMgAl(ox)_3{\cdot}9H_2O$ [33] and $K_3V(ox)_3{\cdot}3H_2O$ [38]. In the $NaMgAl(ox)_3{\cdot}9H_2O$ lattice the rhombic splitting comes primarily from anisotropic H-bonding from the water molecules in the lattice. The rhombic splitting of $[V(ox)_3]^{3-}$, however, is produced by a combination of effects as shown in Fig. 10. One contribution arises from H-bonding between a single oxalate ligand situated in a "H_2O planes" and the other contribution originates in alignment of oxalate ligands with neighboring $[V(ox)_3]^{3-}$ complexes. This second interaction may be responsible for the redshift of the $^1E(^1T_{2g})$ transition to lower energies by ~200 cm^{-1} in $K_3V(ox)_3{\cdot}3H_2O$ compared to $NaMg[Al_{1-x}V_x(ox)_3]{\cdot}9H_2O$ where this apparent π–π stacking of adjacent oxalate ligands is absent (see Fig. 7 and Table 2).

Table 2
Experimental energies of ligand field states and estimated ligand field parameters for selected $V^{III}O_6$ compounds in various trigonal lattices. Crystallographic space groups and site symmetries are given below the complex. All energies are given in cm^{-1}. Observed band polarizations are given in parentheses.

O_h	D_3	Spinor	V^{3+}:Al_2O_3 $R\bar{3}c$, C_3 [1]	$[V(OH_2)_6]^{3+}$ $Pa\bar{3}$, S_6 [4]	$[V(urea)_6]^{3+}$ $R\bar{3}c$, D_3 [2]	α-V(acac)$_3$ Pbca, "D_3" [37]	$[V(ox)_3]^{3-}$ $P2_1/c$, C_1 [38] / $P\bar{3}c1$, C_1 [33]	
	$^3A_2$	A_1	0	0	0	0	0	0
		E	8.25[a]	4.906[f]	5.427	5.524	~4.2	2.99
	^3E	E	992		6.573[j]	9.356[n]	~6.9[r]	11.27[s]
$^3T_{1g}$		E		~1930(10)[g]				
		A_2	1134[b]		~1400[k]	~1100[o]	~700[t]	
		A_1						
$^1T_{2g}$	^1E		9744[b]	~10204(2)[h]	9903(‖,⊥)[l]	–	9403(‖,⊥)[u] / 9592(‖,⊥)[v]	
	$^1A_1$		–	–	–	–	– / –	
^1E_g	^1E		–	–	10073(⊥)[l]	–	–	
$^3T_{2g}$	$^3A_1$		17510(‖)[c]	17570(40)[h]	15547(‖)[l]	18200[p]	16700(‖)[w]	
	^3E		17420(⊥)[c]	19910(80)[h]	16518(⊥)[l]	21100[p]	16910(⊥)[w]	
$^1A_{1g}$	$^1A_1$		21025(⊥)[d]	–	21638(⊥)[l]	–	20758(‖,⊥)[u] / 20465(⊥)[v]	
$^3T_{1g}$(P)	$^3A_2$		24930(‖)[c]	25450(10)[h]	24764(‖)[l]	27400[p]	23575(‖)[w]	
	^3E		25310(⊥)[c]	27780(40)[h]	24740(⊥)[l]	29700[p]		
$^3A_{2g}$	$^3A_2$		31240[c]	–	–	–	~32670(sh,‖)[w]	
	10Dq		18120[e]	18990[h]	17100[l]	~20000[p]	17733[w]	
	v		850[e]	2990 ± 40[i]	1800[l]	2500[i]	~400[x]	
	v'		200[e]	-1590 ± 40[i]	-800[l]	-2100[i]	~450[x]	
	B		590[e]	644[h]	650[l]	684[p]	552.2[w]	
	C		2800[e]	2960[h]	2584[m]	–[q]	3007[w]	
	ζ		164[e]	166.59[h]	150[l]	165[p]	~110[y]	

[a]Far-IR spectroscopy [49]. [b]Low-temperature $^1E(^1T_{2g}) \rightarrow {}^1\Gamma(^3T_{1g})$ emission spectroscopy [56]. [c]Assignments based on the C_{3v} selection rules of the low-temperature polarized electronic absorption spectroscopy in [1] and discussed in [2]. [d]Ref. [16]. [e]Ref. [23]. [f]HFEPR, gelectronic Raman, and hsingle crystal electronic absorption spectroscopy of $Rb[V(OH_2)_6](SO_4)_2{\cdot}6H_2O$ from [30]. [i]Estimated using the experimental splitting of the $^3T_{1g}$(F) and $^3T_{1g}$(P) terms and Eq. (4). [j]HFEPR [13]. [k]Electronic Raman and low temperature $^1E(^1T_{2g}) \rightarrow {}^1\Gamma(^3T_{1g})$ emission spectroscopy [13]. [l]Single crystal polarized electronic absorption spectroscopy of $[V(urea)_6](ClO_4)_3$ from [2]. The authors wrongly assigned the ^1E component of the $^1T_{2g}$ term to a suspect feature at 8420 cm^{-1} in [2], in view of the absence of luminescence from an electronic origin in this region [55]. We thus reassigned the spin-forbidden transitions reported by Dingle et al. [2]. [m]Estimated from the energy of the $^1A_1(^1A_{1g})$ transition and the analytical energy of this transition in [23] using the given values of 10Dq, v, v', and B. [n]HFEPR and [o]MCD spectroscopy [45]. [p]Estimated from magnetic susceptibility measurements [64] and verified by MCD spectroscopy [45]. [q]The value of C is unknown for V(acac)$_3$ due to the fact that no spin-forbidden transition has been reported for this compound. [r,s]Determined from the energy splittings of the non-degenerate $^1A_1$ excited state measured on oriented single crystals of $K_3V(ox)_3{\cdot}3H_2O$ (the average of three different spectroscopic V^{3+} sites) and $NaMg[Al_{1-x}V_x(ox)_3]{\cdot}9H_2O$ (x = 0.015) at 10 K, respectively [14]. [t]Estimated from magnetic susceptibility measurements [42]. [u]Single crystal polarized electronic absorption spectroscopy of $K_3V(ox)_3{\cdot}3H_2O$ ("B" site) and [v]$NaMg[Al_{1-x}V_x(ox)_3]{\cdot}9H_2O$ (x = 0.015) at 10 K. [w]$NaMg[Al_{1-x}V_x(ox)_3]{\cdot}9H_2O$ from ref. [14]. [x]Estimated using the positive axial splitting of the $^3T_{1g}$ ground term of $K_3V(ox)_3{\cdot}3H_2O$ ($\Delta_{ax} \approx +700\ cm^{-1}$) and the $^3T_{2g}$ excited state splitting of $NaMg[Al_{1-x}V_x(ox)_3]{\cdot}9H_2O$ (+210 cm^{-1}) using Eq (4). [y]Estimated using the perturbation expressions given by Eq. (10) assuming no $|\Delta_{rh}|$ contribution to the ZFS for $K_3V(ox)_3{\cdot}3H_2O$.

3.2. Luminescence spectroscopy

Luminescence from the $^1E(^1T_{2g}) \rightarrow {}^3A_2(^3T_{1g})$ spin-forbidden transition of V^{3+}:Al_2O_3, $[V(OH_2)_6]^{3+}$, $[V(urea)_6]^{3+}$, and $NaMg[Al_{1-x}V_x(ox)_3]{\cdot}9H_2O$ compounds have been reported at low temperature [13,15,54–57]. Goldschmidt and co-workers reported the luminescence of V^{3+} in Al_2O_3 in 1965 [58]. The observation of the axial ZFS of the $^3A_2(^3T_{1g})$ ground state in the luminescence spectrum aroused their interest in fabricating a maser at this frequency [58]. Unfortunately their attempts were unsuccessful due to an estimated 3–4 orders of magnitude weaker emission intensity than the R-lines of ruby [58]. The luminescence lifetime of this spin-forbidden transition and below 8 K is ~2–2.5 μs that was reported first by Champagnon and Duval [54] and reconfirmed by Reber and Güdel [56]. The radiative lifetime is estimated to be of the order of 10 ms for this transition at ~9748 cm^{-1}, thus confirming a much lower quantum efficiency for V^{3+} compared to Cr^{3+} in Al_2O_3. Despite this negative aspect of the photophysical properties of these compounds some very interesting and unique spectroscopic features and phenomena have been reported in the low-temperature luminescence of some $V^{III}O_6$ and $V^{III}(\bar{O}\bar{O})_3$ compounds that are discussed in detail below.

Goldschmidt et al. also observed two broad emission bands (fwhm ~1800–2000 cm^{-1}) centered at 17,200 and 25,100 cm^{-1} from V^{3+}:Al_2O_3 with X-ray excitation at low temperature [58]. These transitions were assigned to spin-allowed $^3T_{2g} \rightarrow {}^3A_2(^3T_{1g})$ and $^3T_{1g} \rightarrow {}^3A_2(^3T_{1g})$ bands of V^{3+}:Al_2O_3. The only other observed emission from spin-allowed bands were reported for V^{3+} diluted into YP_3O_9 with an observed luminescence lifetime at 8 K of 5 μs, roughly twice as long as for V^{3+}:Al_2O_3 at the same temperature [56]. An additional weak shoulder was also observed for V^{3+}:Al_2O_3 by Goldschmidt et al. centered at ~15,900 cm^{-1} that was tentatively assigned to emission from the $^3T_{2g}$ excited state to the upper trigonal component of the $^3T_{1g}$ ground state, $^3E(^3T_{1g})$ [58]. This was the first spectroscopic evidence of the magnitude of the trigonal splitting of the $^3T_{1g}$ ground state of Δ_{ax} ~1300 ± 100 cm^{-1}. Reber and Güdel reinvestigated the $^1E(^1T_{2g}) \rightarrow {}^3A_2(^3T_{1g})$ emission of V^{3+}:Al_2O_3 to lower energies and this is shown in Fig. 11a. In addition to the sharp emission of the electronic origin with negligible Stokes shift they also detected a broad emission centered at ~1130 cm^{-1} lower in energy [56]. There are no reported vibrational side bands in this energy range. This energy difference is similar to the value of Δ_{ax} = ~960–1200 cm^{-1} (1) estimated by fitting the energies of the polarized spin-allowed bands in Fig. 5a by Macfarlane [9], (2) by analyzing the intensity profiles of the spin-allowed transitions up to 1300 K by McClure [1], and (3) by estimating the Δ_{ax} value using the experimental splitting of the $^3A_2(^3T_{1g}) \rightarrow {}^1A_1(^1A_{1g})$ of $D \approx 8\ cm^{-1}$ and using $\lambda = 70\ cm^{-1}$ in

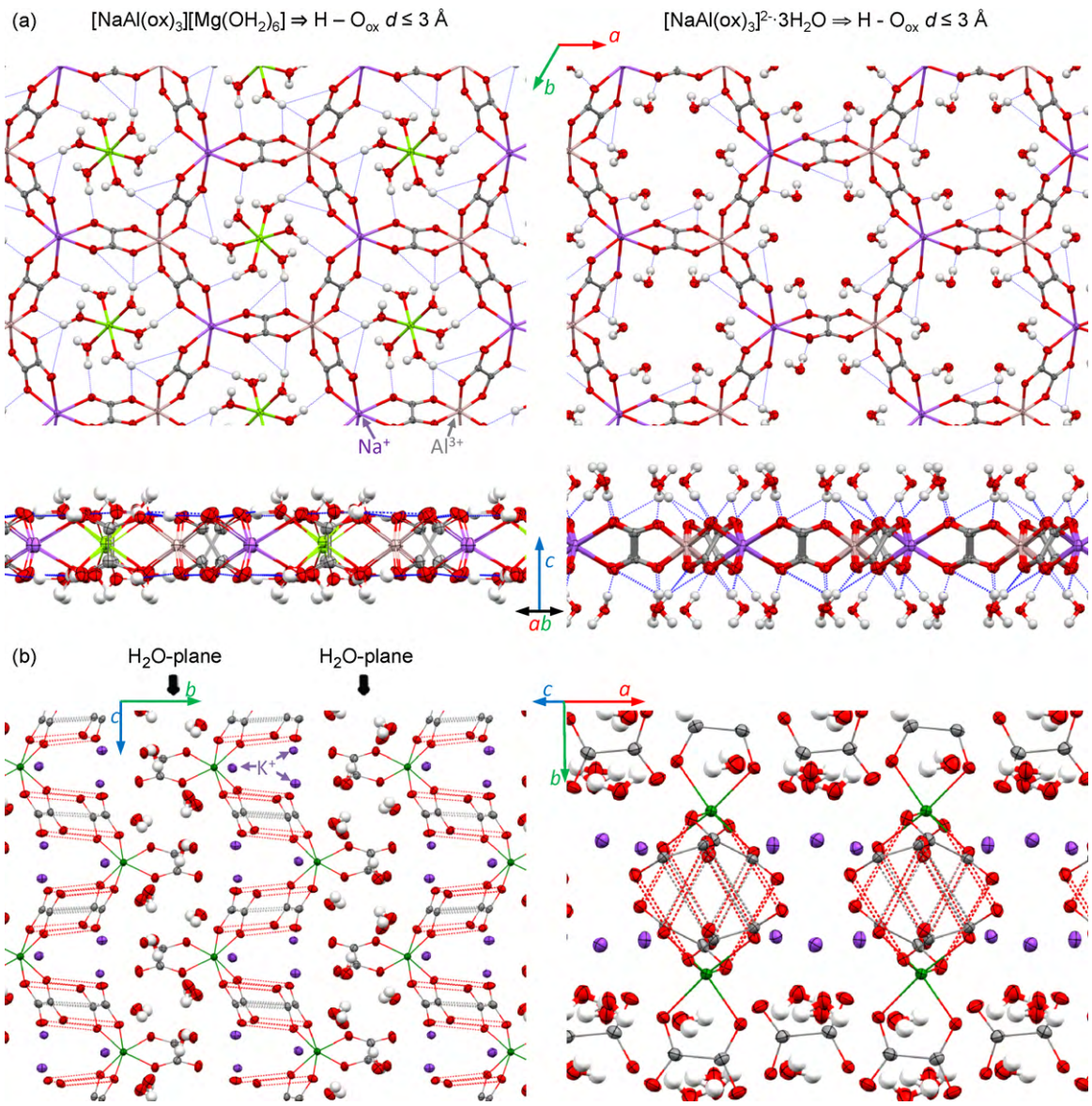

Fig. 10. Crystal packing and H-bonding of (a) $NaMgAl(ox)_3{\cdot}9H_2O$ [33] and (b) $K_3V(ox)_3{\cdot}3H_2O$ [38]. The views of $NaMgAl(ox)_3{\cdot}9H_2O$ are divided into interactions between the $[NaCr(ox)_3]^{2-}$ honeycomb lattice and waters coordinated to Mg^{2+} (bound waters in the void of the honeycomb, left) and free waters (above and below the honeycomb, right). The top views in (a) are down the crystal *c*-axis and the bottom views in (a) are in the *ab*-plane. Only H–O_{ox} contact distances of <2.9 Å are shown with dotted H-bonds. (b, left) View of $K_3V(ox)_3{\cdot}3H_2O$ down the crystal *a*-axis (pseudo-D_3 molecular axis). The water molecules are found in planes running along *ac*-planes and interact mainly with only one of the oxalate ligands. The other "unperturbed" oxalate ligands align with the oxalate ligands of neighboring $[V(ox)_3]^{3-}$ complexes in a semi-supramolecular arrangement. The distance between oxalate ligands shown with dashed lines is ~3.3 Å. The angle V^{III}–(CC)–(CC)′ is 119.33° where (CC) is the center of gravity between the carbons of the oxalate ligands and the prime accent denotes an oxalate ligand of an adjacent $[V(ox)_3]^{3-}$ complex. The packing between takes place along the [10–1] direction of the crystal shown in the right hand side of (b).

Eq. (10) [8]. This observed emission was thus assigned to the $^1E(^1T_{2g}) \rightarrow {}^3E(^3T_{1g})$ transition [56]. It is weak and individual splittings between the individual spinors of the ^3E trigonal component were not resolved in the spectrum at temperatures down to 8 K.

The emission spectrum of $[V(urea)_6]^{3+}$ was first reported by Flint and Greenough in the neat iodide salt [55]. The emission spectra of the iodide and perchlorate salts have been recently reinvestigated by Beaulac and Reber and co-workers to lower energies in search of emission from the lowest energy electronic origin to the ^3E state [36,57], similar to that observed in V^{3+}:Al_2O_3. They indeed observed a broad, temperature dependent feature at ~1400 cm^{-1} lower in energy than the electronic origin (see Fig. 11b). However, the feature is surrounded by vibronic side bands. The Raman spectra of the protonoated and deuterated, $[V(urea\text{-}d_4)_6](ClO_4)_3$, salts provided unambiguous spectroscopic evidence for assignment of this feature to the $^1E(^1T_{2g}) \rightarrow {}^3E(^3T_{1g})$ emission (*vide infra* [36]). During our studies we measured the luminescence lifetimes of the $^1E(^1T_{2g}) \rightarrow {}^3A_2(^3T_{1g})$ transition of $[V(urea)_6]^{3+}$ with a 20% doping level in an $[Al(urea)_6]I_3$ single crystal and present them in Fig. 11d. The almost linear decrease in lifetime with increasing temperature is similar to the behavior of V^{3+}:Al_2O_3 [54], also shown in Fig. 11d.

We recently reported the temperature dependence of the emission from $[V(ox)_3]^{3-}$ diluted in $NaMgAl(ox)_3{\cdot}9H_{2-y}D_yO$ where *y* is between 1 and 2 [15]. The emission spectrum of a 2.9% crystal grown from a solution of 50:50 H_2O:D_2O is shown in Fig. 11c. Despite the apparent lack of symmetry and large rhombic splitting of the $[V(ox)_3]^{3-}$ complex in this lattice as shown in Fig. 7d, we were able to detect a weak luminescent signal in the near-IR region. However, we were unable to detect any emission to any of the upper components of the $^3T_{1g}$ ground state in this lattice as seen

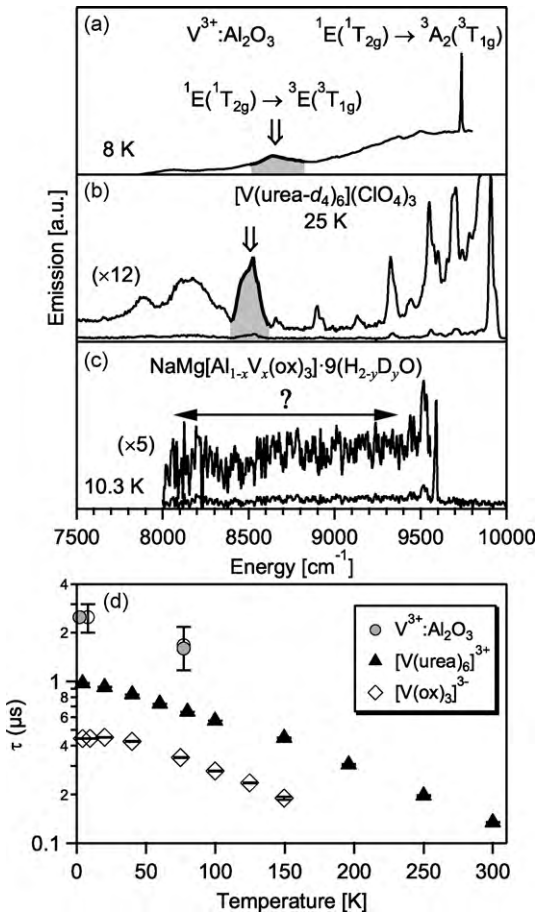

Fig. 11. Low-temperature overview emission spectra of (a) V^{3+}:Al_2O_3 at 8 K, (b) $[V(urea\text{–}d_4)_6](ClO_4)_3$ at 25 K, and (c) $NaMg[Al_{1-x}V_x(ox)_3]\cdot 9(H_{2-y}D_yO)$ ($x = 0.029$, $y = 1$) at 10.3 K. Spectra in (a) and (b) were digitized from Refs. [56,36], respectively. Some of the spectrum in (c) was presented in ref. [15]. (d) Luminescence lifetimes (log scale) of the $^1E(^1T_{2g}) \rightarrow {}^3\Gamma(^3T_{1g})$ (Γ is the lowest energy component of the $^3T_{1g}$ ground state) as a function of temperature for V^{3+}:Al_2O_3 from refs [54] (filled circles) and [56] (open circles), $[Al_{1-x}V_x(urea)_6]I_3$ ($x = 0.2$) [50], and $NaMg[Al_{1-x}V_x(ox)_3]\cdot 9(H_{2-y}D_yO)$ ($x = 0.029$, $y = 1$) [15].

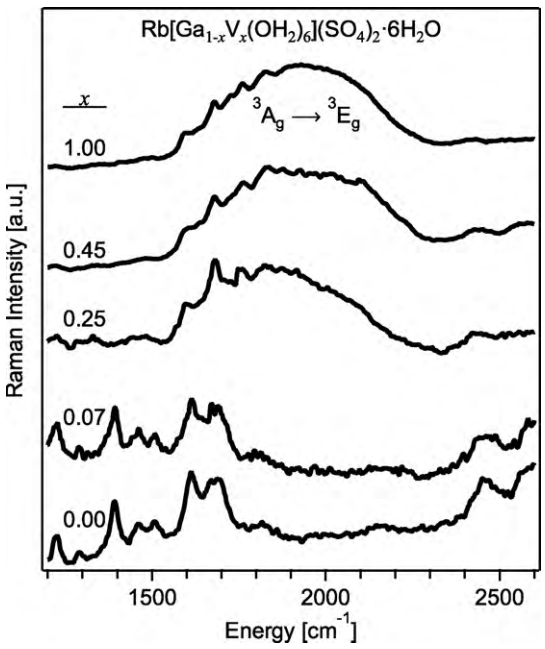

Fig. 12. Raman spectra of $Rb[Ga_{1-x}V_x(OH_2)_6](SO_4)_2\cdot 6(H_2O)$ single crystals with $x = 1$, 0.45, 0.25, 0.07, and 0 from top to bottom. The Raman spectra were collected in the $X'(ZZ)Y'$ orientation ($A_g + E_g$ modes active) with 457.9 nm excitation from an Ar ion laser [63]. Collection temperature was 80 K. Spectra were digitized from ref. [30], with permission of the copyright holders.

in Fig. 11c. The narrow band did display a splitting nearly equal to the axial ZFS with no detectable Stokes shift [15]. The luminescence lifetime of the crystal shown in Fig. 11c was constant below 20 K with ~0.45 μs. Above this temperature the lifetime displays a linear decrease with increasing temperature similar to the other $V^{III}O_6$ compounds shown in Fig. 11d. The measured lifetime of a crystal with ~5% doping grown from pure D_2O increased to ~0.79 μs at 4 K [15]. This demonstrates that the luminescence lifetime of $[V(ox)_3]^{3-}$ in $NaMgAl(ox)_3\cdot 9(H_{2-y}D_yO)$ is much more sensitive to changes in y, that is, coupling to high-frequency O–H vibrations, than to self-quenching effects with increasing vanadium concentration.

3.3. Electronic Raman spectroscopy

Electronic transitions involving metal ions with components from orbitally-degenerate ground terms, such as between the $^3A \leftrightarrow {}^3E$ trigonal components, Δ_{ax} in Eq. (8), of pseudo-octahedral V^{3+} are Raman active [59]. Such electronic transitions in the Raman spectra of $V^{III}O_6$ compounds were first observed for the cesium and guanidinium $[V(OH_2)_6]^{3+}$ alums in the β modification at ~2000 cm^{-1} by Best and Clark [60]. Previous to direct observation of the energy of Δ_{ax} in $V^{III}O_6$ compounds by this technique or by luminescence spectroscopy as described above, this quantity was estimated by fitting of the magnetic susceptibility, which was shown to be over-parameterized and very sensitive to the spin–orbit coupling value $A\lambda$ used in Eq. (8) and therefore not very accurate [60].

In a strictly trigonal field the width of the ^3E electronic Raman transition is ~$2A\lambda$, which is much broader than any of the Raman active vibrational bands [60]. Additional studies by Tregenna-Piggott and co-workers extended the use of electronic Raman spectroscopy to study other $[V(OH_2)_6]^{3+}$ alums with different counterions and full deuteration of the water molecules [30–32]. Fig. 12 shows the 80 K polarized Raman spectra from 1200–2600 cm^{-1} of $Rb[Ga_{1-x}V_x(OH_2)_6](SO_4)_2\cdot 6H_2O$ single crystals for x values covering the entire range from 0 to 1 [30]. The spectra show a broad feature centered at ~2000 cm^{-1} that decreases in intensity with decreasing vanadium concentration in the crystal. Below 7% vanadium concentration the broad feature is occluded by the Raman active lattice vibrations. This dataset provides unambiguous proof of the assignment of the transition at ~2000 cm^{-1} to an electronic transition between the trigonal components of the $^3T_{1g}$ ground state.

Tregenna-Piggott et al. analysed the large body of experimental work focusing on the electronic structure of $[V(OH_2)_6]^{3+}$ in the β-alums with the aid of the angular overlap model [3–5,30–32,61]. They found the very large trigonal splitting in these compounds to be primarily the result of anisotropic π-bonding influenced by the orientation of the water molecules in the various lattices (see Fig. 13). The electronic structure of V^{3+} in the alums is dominated by the interaction from the π-orbitals situated perpendicular to the V–OH_2 plane ($e_{\pi\perp}$) with no influence from the π-orbitals parallel to the plane ($e_{\pi||}$). This bonding motif has been extended to all of the $[V(OH_2)_6]^{3+}$ β-alums studied by Tregenna-Piggott et al. and was also applied to the electronic structure of $[V(urea)_6](ClO_4)_3$ [36].

Further aspects of the bandshapes and splittings of the electronic Raman transitions in some β-alums have been observed and thoroughly accounted for by invoking a dynamic JT effect of the ^3E_g state [3,31]. Carver, Spichiger and Tregenna-Piggott demon-

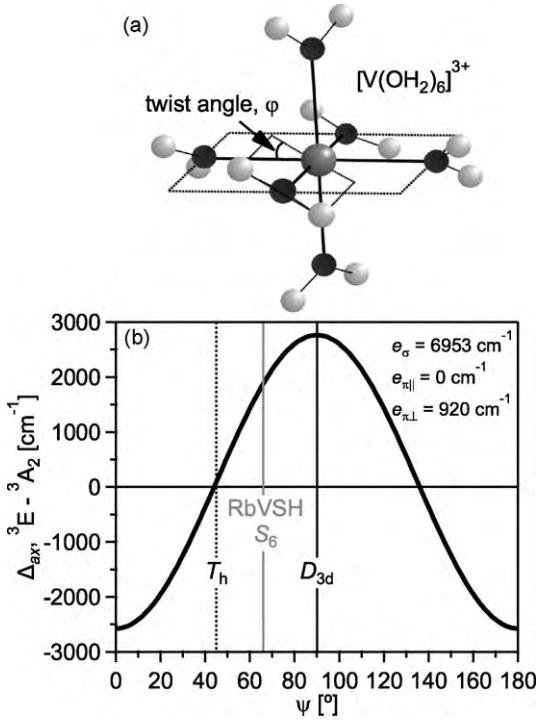

Fig. 13. (a) Stereochemistry and definition of the twist angle of the H_2O molecule with respect to the arbitrary equatorial plane. This angle is defined with respect to a D_4 axis, but the Euler angle for a trigonal distortion are described with respect to one of the C_3 molecular symmetry axes of an octahedron. Therefore, this twist angle is not the ψ angle for $[V(OH_2)_6]^{3+}$. Panel (a) was modified from ref. [61], with permission from the copyright holders. (b) Calculated Δ_{ax} splitting behavior with concerted rotation of the bound H_2O molecules using input angular overlap model parameters shown in the panel with input geometries for $Rb[V(OH_2)_6](SO_4)_2{\cdot}6H_2O$ (RbVSH using Tregenna-Piggott's nomenclature) determined crystallographically in ref. [4]. The Euler angles and Racah parameters used in the calculation and given in [4] are: $\theta = 55.28^\circ$, $\varphi = 60^\circ$, $B = 644\,cm^{-1}$, $C = 2963\,cm^{-1}$ and $\zeta = 0$. The experimental value of ψ value for RbVSH is $\psi = 66.45^\circ$ is shown by the vertical green line.

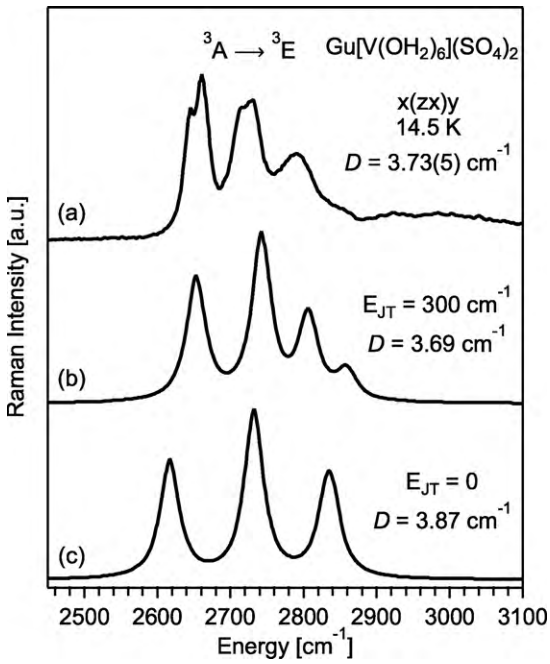

Fig. 14. (a) Experimental and (b and c) calculated Raman spectra showing the $^3A \rightarrow {}^3E$ electronic transition of $Gu[V(OH_2)_6](SO_4)_2$. The E_{JT} parameter in the calculated spectra in (b) and (c) is the Jahn–Teller stabilization energy. For more information regarding the details of JT effect and construction of the Hamiltonian used to calculate the spectra in (b) and (c) see Ref. [31]. The spin–orbit coupling parameter, λ, used to calculate both (b) and (c) was $107\,cm^{-1}$. Spectra were digitized from Ref. [31].

strated that the pure ligand field analysis was unable to adequately describe the axial splitting of the $^3A_g(^3T_{1g})$ ground state in light of the electronic Raman spectrum of $Gu[V(OH_2)_6](SO_4)_2$ where Gu is the guanidinium cation, $[C(NH_2)_3]^+$ (see Fig. 14, [31]). The unique features of this particular lattice are that individual spinors are nicely resolved and thereby give estimates of both $\Delta_{ax} = 2720\,cm^{-1}$ and $A\lambda \approx 70\,cm^{-1}$. The perturbation expression given for the scenario when $\Delta_{ax} \gg A\lambda$ is given by Eq. (10), which yields a calculated axial ZFS of $D \approx 1.8\,cm^{-1}$. This value of D is roughly 50% of the value determined by HFEPR spectroscopy of $D = 3.58\,cm^{-1}$ [4]. As noted by the authors in the title of Ref. [31], this observation is the "quintessential manifestation of the dynamical Jahn–Teller effect". The apparent reduction in the spin–orbit parameter is thus not real but the result of the Ham effect [31]. The impact of this effect on the electronic structure of the ground state is clear; however, we believe that it has another important effect on the non-radiative decay pathways of $V^{III}O_6$ and $V^{III}(\bar{O}\bar{O})_3$ compounds that will be presented and discussed in Section 4.1.

Electronic Raman transition between the trigonal components at 1400 and $1600\,cm^{-1}$ have also been observed for the anhydrous V^{3+} sulfates such as $CsV(SO_4)_2$ and $KV(SO_4)_2$, respectively [62]. The authors determined the sign of the Δ_{ax} parameter by analyzing the splittings of the trigonal components of the $^3T_{1g} \rightarrow {}^3T_{2g}$ and $^3T_{1g} \rightarrow {}^3T_{1g}(P)$ spin-allowed transitions that were deconvoluted from the unpolarized electronic absorption spectra. These splittings were not well resolved and based on the expected isotropic π-bonding from the sulfate ions with T_d symmetry, it might be worthwhile reinvestigating the electronic ground state of these compounds using a direct probe of the ZFS or magnetic susceptibility down to 2 K to confirm the sign of the trigonal splitting of the ground state.

The electronic Raman spectra of the $[V(urea)_6]^{3+}$ complex has been recently reinvestigated by the Beaulac, Reber and co-workers [36,57]. In Ref. [36], the protonated and deuterated perchlorate salts were measured and showed a broad electronic Raman transition at $\sim 1400\,cm^{-1}$ that unambiguously confirmed their assignment the feature in the 25 K luminescence spectrum to the $^1E(^1T_{2g}) \rightarrow {}^3E(^3T_{1g})$ transition (see Fig. 11). Unfortunately, the electronic Raman spectra did not show resolved splittings, but we see no reason to doubt that the dynamical JT effect is present to some degree in the $[V(urea)_6]^{3+}$ compounds as well.

4. Photophysics of $V^{III}O_6$ and $V^{III}(\bar{O}\bar{O})_3$ compounds

The spin-forbidden near-IR emission of V^{3+} in the various pseudo-octahedral lattices shown in Fig. 11 and discussed in Section 3.2 decays rapidly with an estimated quantum efficiency of the order of only 10^{-4} to 10^{-5} even at lowest temperatures [15]. In the next section we review the various mechanisms that have been proposed to account for this low efficiency for $V^{III}O_6$ and $V^{III}(\bar{O}\bar{O})_3$ compounds.

4.1. Deactivation mechanisms

Different mechanisms have been proposed for the efficient quenching of the spin-forbidden emission in $V^{III}O_6$ and $V^{III}(\bar{O}\bar{O})_3$ compounds. The most studied lattice, $V^{3+}:Al_2O_3$, has phonon modes at $\sim 1000\,cm^{-1}$ that Reber and Güdel invoked in their analysis that a multi-phonon deactivation pathway was solely responsible for the low quantum efficiency [56]. Champagnon and Duval argued for an alternative pathway that included coupling of a JT effect in the upper ^3E trigonal component of the $^3T_{1g}$ ground state

mixing with the emitting ^1E state via spin–orbit coupling [54]. However, at the time of those studies there was no direct evidence for a JT effect in the ^3E state of V^{3+}:Al_2O_3, and Reber and Güdel were somewhat skeptical towards that mechanism [56]. Today, the unambiguous observation of a dynamic JT effect in $[V(OH_2)_6]^{3+}$ β-alums by Tregenna-Piggott and co-workers [31] gives us reason to assume that the effect is most likely active also in varying degrees in V^{3+}:Al_2O_3 as well as in other pseudo-octahedral $V^{III}O_6$ and $V^{III}(\bar{O}\bar{O})_3$ compounds.

The rationale formulated by Champagnon and Duval adequately explains the efficient non-radiative pathways including a dynamic JT effect of the $^3E(^3T_{1g})$ state that we believe is general to pseudo-octahedral $V^{III}O_6$ and $V^{III}(\bar{O}\bar{O})_3$ compounds [54]. Additionally, when the energies of the phonon mode and Δ_{ax} splitting of the $^3T_{1g}$ ground state are similar the intensities of vibrational overtones can be greatly enhanced as shown by Tregenna-Piggott and Carver for the case of the β-alums [3]. The high-frequency quenching vibrational modes and $^3E(^3T_{1g})$ terms are in close energetic proximity for the V^{3+} ion in both Al_2O_3 and hexa-urea lattices [36]. We therefore also suspect some contribution to the non-radiative decay by a JT active distortion of the $^3E(^3T_{1g})$ state as well in the $[V(urea)_6]^{3+}$ compounds. Indeed, the Δ_{ax} splitting energy and high-frequency lattice phonons are larger for $[V(urea)_6]^{3+}$ than V^{3+}:Al_2O_3, which accounts for the lower luminescence lifetimes for $[V(urea)_6]^{3+}$ as given in Fig. 11d.

For $NaMg[Al_{1-x}V_x(ox)_3]\cdot 9H_2O$, we showed that the axial ZFS component is negative suggesting a ^3E ground state that is further split by a rhombic field (see Section 2.2 and Fig. 3 and [14]). The observed luminescence lifetimes shown in Fig. 11c are lowest for V^{3+} in the $NaMgAl(ox)_3\cdot 9H_2O$ lattice. In view of the large rhombic contribution to the ZFS of the $^3T_{1g}$ ground state we are cautious to invoke the JT effect to explain the inefficient luminescence from $[V(ox)_3]^{3-}$. The magnitude of the rhombic splitting of V^{3+} in $NaMgAl(ox)_3\cdot 9H_2O$ is $|\Delta_{rh}| \approx 250\,cm^{-1}$ [14], which is comparable in magnitude to the JT stabilization energy of the ^3E state in $Gu[V(OH_2)_6](SO_4)_2$ [31]. The combination of these effects enhance the non-radiative decay pathways as observed experimentally in Fig. 11c. Perhaps our prediction of a $^3E(^3T_{1g})$ ground state for $[V(ox)_3]^{3-}$ will motivate future studies on the nature of the JT effect in $[V(ox)_3]^{3-}$ coordination compounds.

5. Conclusions

Trivalent vanadium in pseudo-octahedral oxygen coordination presents many challenges to the coordination chemist. We have reviewed the literature and presented evidence demonstrating that the second coordination sphere can have important effects on the electronic structure, especially of the $^3T_{1g}$ ground state of $[V(OH_2)_6]^{3+}$ and $[V(ox)_3]^{3-}$ complexes. The ability to directly detect the axial splitting of the $^3T_{1g}$ ground state by electronic Raman or luminescence spectroscopy allows for key magneto-structural correlations to be made as in the $[V(OH_2)_6]^{3+}$ β-alums studied by Tregenna-Piggott and colleagues. The ability to exploit these magneto-structural correlations in the rational design of new magnetic materials with predictable properties will continue to be a major challenge to the coordination chemist.

Experimental evidence of other interesting phenomena including the dynamic JT effect in the upper $^3E(^3T_{1g})$ state of $Gu[V(OH_2)_6](SO_4)_2$ forces us to reconsider the implications that such an effect has on the overall low luminescence quantum efficiency of the near-IR $^1E(^1T_{2g}) \rightarrow {}^3\Gamma(^3T_{1g})$ spin-forbidden emission of other $V^{III}O_6$ and $V^{III}(\bar{O}\bar{O})_3$ complexes and other coordination compounds involving chromophores with orbitally degenerate ground states We hope that this review highlights the wealth of knowledge of the electronic structure of V^{3+} complexes that can be obtained by detailed analysis of low-temperature polarized electronic absorption, luminescence and Raman spectroscopies.

Acknowledgements

We thank the Swiss National Science Foundation (grant number 200020-125175) for financial support. Dr. Philip Tregenna-Piggott is acknowledged for helpful discussions.

References

[1] D.S. McClure, J. Chem. Phys. 36 (1962) 2757.
[2] R. Dingle, P.J. McCarthy, C.J. Ballhausen, J. Chem. Phys. 50 (1969) 1957.
[3] P.L.W. Tregenna-Piggott, G. Carver, Inorg. Chem. 43 (2004) 8061.
[4] P.L.W. Tregenna-Piggott, D. Spichiger, G. Carver, B. Frey, R. Meier, H. Weihe, J.A. Cowan, G.J. McIntyre, G. Zahn, A.L. Barra, Inorg. Chem. 43 (2004) 8049.
[5] P.L.W. Tregenna-Piggott, H. Weihe, J. Bendix, A.L. Barra, H.U. Güdel, Inorg. Chem. 38 (1999) 5928.
[6] T.S. Piper, R.L. Carlin, J. Chem. Phys. 33 (1960) 608.
[7] T.S. Piper, R.L. Carlin, J. Chem. Phys. 35 (1961) 1809.
[8] M.H.L. Pryce, W.A. Runciman, Disc. Faraday Soc. 26 (1958) 34.
[9] R.M. Macfarlane, J. Chem. Phys. 40 (1964) 373.
[10] F.E. Mabbs, D.J. Machin, Magnetism and Transition Metal Complexes, Chapman and Hall, London, 1973.
[11] J. Pontnau, R. Adde, Phys. Rev. B 14 (1976) 3778;
C. Rudowicz, Y.-Y. Yeung, Z.-Y. Yang, J. Qin, J. Phys.: Condens. Matter 14 (2002) 5619.
[12] M. Dong-ping, M. Xiao-dong, C. Ju-rong, L. Yan-yun, Phys. Rev. B 56 (1997) 1780.
[13] R. Beaulac, P.L.W. Tregenna-Piggott, A.-L. Barra, H. Weihe, D. Luneau, C. Reber, Inorg. Chem. 45 (2006) 3399.
[14] K.R. Kittilstved, L.A. Sorgho, N. Amstutz, P.L.W. Tregenna-Piggott, A. Hauser, Inorg. Chem. 48 (2009) 7750.
[15] K.R. Kittilstved, A. Hauser, J. Lumin. 129 (2009) 1493.
[16] S. Sakatsume, E. Kanda, Sci. Rep. Res. Inst., Tohoku Univ., Ser. A Suppl 18 (1966) 514.
[17] S. Sakatsume, I. Tsujikawa, J. Phys. Soc. Jpn. 19 (1964) 1080.
[18] C.J. Ballhausen, Introduction to Ligand Field Theory, McGraw-Hill, New York, 1962.
[19] E. König, S. Kremer, Ligand Field Energy Diagrams, Plenus Press, New York, NY, 1977.
[20] S. Sugano, Y. Tanabe, J. Phys. Soc. Jpn. 13 (1958) 880.
[21] A.D. Liehr, J. Phys. Chem. 64 (1960) 43.
[22] H.U. Rahman, J. Phys. C 4 (1971) 3301;
H.U. Rahman, W.A. Runciman, J. Phys. C 4 (1971) 1576.
[23] J. Pontnau, R. Adde, J. Phys. (Paris) 37 (1976) 603.
[24] Y. Tanabe, S. Sugano, J. Phys. Soc. Jpn. 9 (1954) 753.
[25] M. Atanasov, C.A. Daul, C. Rauzy, Chem. Phys. Lett. 367 (2003) 737.
[26] J. Ferguson, D.L. Wood, Aust. J. Chem. 23 (1970) 861.
[27] H. Adamsky, T. Schoenherr, M. Atanasov, Comp. Coord. Chem. II 2 (2004) 661.
[28] J. Bendix, Compr. Coord. Chem. II 2 (2004) 673.
[29] P.L.W. Tregenna-Piggott, MagProp (Part of the NIST DAVE Software Suite), v2.0, 2008, http://www.ncnr.nist.gov/dave (20 October 2008).
[30] P.L.W. Tregenna-Piggott, S.P. Best, H.U. Güdel, H. Weihe, C.C. Wilson, J. Solid State Chem. 145 (1999) 460.
[31] G. Carver, D. Spichiger, P.L.W. Tregenna-Piggott, J. Chem. Phys. 122 (2005) 124511.
[32] D. Spichiger, G. Carver, C. Dobe, J. Bendix, P.L.W. Tregenna-Piggott, R. Meier, G. Zahn, Chem. Phys. Lett. 337 (2001) 391.
[33] H. Riesen, A.D. Rae, Dalton Trans. (2008) 4717.
[34] M.A. Atanasov, T. Schonherr, H.H. Schmidtke, Theor. Chim. Acta 71 (1987) 59.
[35] L.E. Orgel, J. Chem. Soc. (1961) 3683.
[36] R. Beaulac, P.L.W. Tregenna-Piggott, A.L. Barra, H. Weihe, D. Luneau, C. Reber, Inorg. Chem. 45 (2006) 3399.
[37] S.J. Kavitha, K. Panchanatheswaran, J.N. Low, C. Glidewell, Acta Cryst. E61 (2005) m1326.
[38] K.S. Min, A.L. Rhinegold, J.S. Miller, Inorg. Chem. 44 (2005) 8433.
[39] J. Krzystek, A. Ozarowski, J. Telser, Coord. Chem. Rev. 250 (2006) 2308.
[40] R. Boča, Coord. Chem. Rev. 248 (2004) 757.
[41] R. Boča, Struct. Bond. 117 (2006) 1.
[42] D.J. Machin, K.S. Murray, J. Chem. Soc. A (1967) 1498.
[43] B.N. Figgis, J. Lewis, F. Mabbs, J. Chem. Soc. (1960) 2480.
[44] A. Abragam, M.H.L. Pryce, Proc. R Soc. London A 205 (1951) 135.
[45] J. Krzystek, A.T. Fiedler, J.J. Sokol, A. Ozarowski, S.A. Zvyagin, T.C. Brunold, J.R. Long, L.-C. Brunel, J. Telser, Inorg. Chem. 43 (2004) 5645.
[46] B.N. Figgis, M.A. Hitchman, Ligand Field Theory and its Applications, Wiley–VCH, New York, 2000.
[47] P.J. Stephens, M. Lowe-Pariseau, Phys. Rev. 171 (1968) 322;
J.A. Spencer, J. Chem. Phys. 54 (1971) 5139;
W.C. Scott, M.D. Sturge, Phys. Rev. 146 (1966) 262.

[48] Line shape analysis determined by deconvolution using Voigt band profiles and fixing the energies of the transitions to the fitted values in the 0.5 cm^{-1} resolution spectrum. The inhomogeneous line widths were assumed the same for the two transitions for the line shape analysis.
[49] R.R. Joyce, P.L. Richards, Phys. Rev. 179 (1969) 375.
[50] K.R. Kittilstved, A. Hauser, unpublished results.
[51] R.D. Shannon, Acta Cryst. A 32 (1976) 751.
[52] B.N. Figgis, L.G.B. Wadley, J. Chem. Soc., Dalton Trans. (1972) 2182.
[53] O.S. Mortensen, J. Chem. Phys. 47 (1967) 4215.
[54] B. Champagnon, E. Duval, J. Phys. Lett. 38 (1977) 299.
[55] C.D. Flint, P. Greenough, Chem. Phys. Lett. 16 (1972) 369.
[56] C. Reber, H.U. Güdel, Chem. Phys. Lett. 154 (1989) 425.
[57] R. Beaulac, J.C. Tremblay, G. Bussière, C. Reber, Can. J. Anal. Sci. Spect. 46 (2001) 152.
[58] Z. Goldschmidt, W. Low, M. Foguel, Phys. Lett. 19 (1965) 17.
[59] R.J.H. Clark, T.J. Hines, in: R.J.H. Clark, R.E. Hester (Eds.), Advances in Infrared and Raman Spectroscopy, vol. 9, Heyden, London, 1982, p. 282;
J.A. Koningstein, Annu. Rev. Phys. Chem. 24 (1973) 121.
[60] S.P. Best, R.J.H. Clark, Chem. Phys. Lett. 122 (1985) 401.
[61] S. Dolder, D. Spichiger, P.L.W. Tregenna-Piggott, Inorg. Chem. 42 (2003) 1343.
[62] R.W. Berg, S. Boghosian, N.J. Bjerrum, R. Fehrmann, B. Krebs, N. Sträter, O.S. Mortensen, G.N. Papatheodorou, Inorg. Chem. 32 (1993) 4714;
R. Ferhrmann, B. Krebs, G.N. Papatheodorou, R. Berg, N.J. Bjerrum, Inorg. Chem. 25 (1986) 1571.
[63] P.L.W. Tregenna-Piggott, private communication.
[64] A.K. Gregson, D.M. Doddrell, P.C. Healy, Inorg. Chem. 17 (1978) 1216.